Cold Regions Research and Engineering Laboratory

US Army Corps of Engineers®
Engineer Research and
Development Center

Pavement Subgrade Performance Study

Project Overview

Vincent Janoo, Lynne Irwin, and Robert Haehnel

March 2003

Pavement Subgrade Performance Study

Project Overview

Vincent Janoo

Cold Regions Research and Engineering Laboratory
72 Lyme Road
Hanover, New Hampshire 03755

Lynne Irwin

Cornell University Local Roads Program
Ithaca, New York

Robert Haehnel

Cold Regions Research and Engineering Laboratory
72 Lyme Road
Hanover, New Hampshire 03755

ABSTRACT

Mechanistic design or evaluation of pavements requires fundamental material properties and material failure criteria as a function of load and environmental effects such as temperature and moisture content. The strength or weakness of a pavement structure is based on the performance of the subgrade. The current subgrade failure criteria used in many mechanistic design/evaluation methodologies were surmised mainly from tests that did not consider the effects of subgrade soil type or moisture content. Because of these limitations the current FHWA-sponsored Subgrade Performance Study was designed to investigate and upgrade the failure criteria of subgrade materials. The project plans to study the effect of subgrade type and moisture content on the failure criteria. This international study includes testing at the U.S. Army Cold Regions Research and Engineering Laboratory, where test sections are being constructed using four subgrade types and three moisture contents and subjected to accelerated loading. The sections are instrumented with stress, strain, moisture, and temperature sensors. In this study the ambient temperature is held at around 20°C. This report provides an overview of the test program and testing procedure. Subsequent reports will detail the construction of each test section, the data acquired, and the results.

CONTENTS

LIST OF ILLUSTRATIONS

LIST OF TABLES

CONVERSION FACTORS, NON-SI TO SI UNITS OF MEASUREMENT

Non-SI units of measurement used in this report can be converted to SI units as follows:

Multiply	By	To Obtain
feet	0.3048	meters
cubic inches	16.39	cubic centimeters
pounds per cubic foot	16.0185	kilograms per cubic meter
mph	0.447047	m/s
gallons (U.S. liquid)	0.003785412	cubic meters
ounces	28.35	grams
pounds (force)	4.448222	newtons
psi	6895.00	pascals
square feet	0.09290304	square meters
cubic yards	0.02832	cubic meters
tons (2,000 pounds, mass)	907.1847	kilograms
[1] To obtain Celsius (C) temperature readings from Fahrenheit (F) readings, use the following formula: C = (5/9)(F – 32). To obtain kelvin (K) readings, use: K = (5/9)(F – 32) + 273.15.		

PREFACE

Pavement Subgrade Performance Study: Project Overview

VINCENT JANOO, LYNNE IRWIN, AND ROBERT HAEHNEL

1   INTRODUCTION

Since the mid-1960s, pavement researchers have been refining mechanistically based design methods. While the mechanics of layered systems are well developed, there remains much work to be done in the areas of material characterization and failure criteria. With respect to asphalt concrete pavements, the current failure criteria used are the horizontal tensile strain at the bottom of the asphalt concrete layer and the vertical strain at the top of the subgrade layer (Fig. 1).
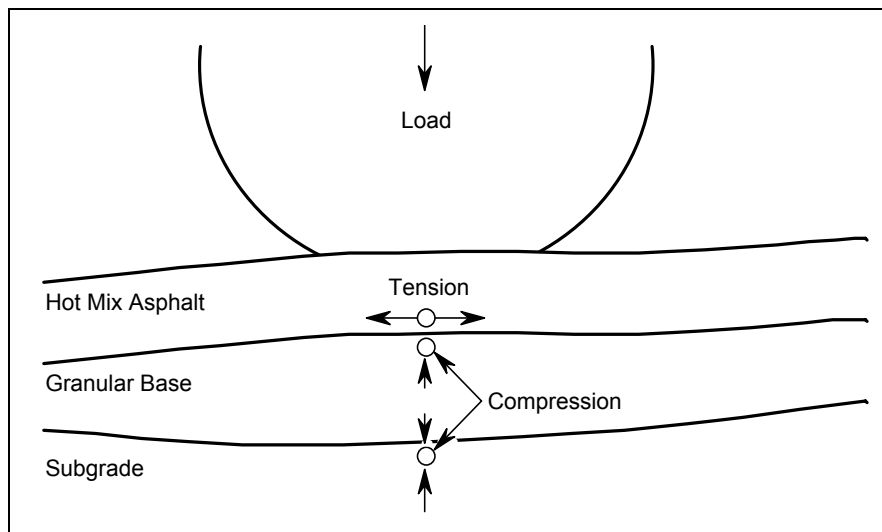
Figure 1. Tensile and compressive strains in flexible pavements. (After Huang 1993.)

The horizontal strain is used to predict and control fatigue cracking in the surface layer. Similarly the vertical strain at the top of the subgrade is used to predict and control permanent deformation (rutting) of the pavement structure

caused by shear deformation in the upper subgrade. While test methods and failure criteria for predicting fatigue cracking are maturing, there has been very little effort placed on the refinement of the subgrade failure criteria. The development of the current subgrade failure criteria, which limits the amount of vertical strain on top of the subgrade, is based primarily on limited data from the AASHO Road Test (Dormon and Metcalf 1965).

2 AASHO ROAD TEST

Between 1950 and 1960 there were three full-scale road tests performed to determine the effect of axle loads on pavements and to develop rational design procedures. The first, Road Test 1-MD (1950), was conducted to determine the effect of specific axle loads at known speeds and frequencies on then-existing rigid pavements. The second, the WASHO Road Test, conducted in southern Idaho in 1953 and 1954, was used to develop load limits for flexible pavements and a rational flexible pavement design method. The third, the AASHO Road Test (1956–1960), was conducted near Ottawa, Illinois (Highway Research Board 1962). The rationale for this test program was to develop a pavement design procedure applicable to both flexible and rigid pavements. The results from the AASHO Road Test were used to determine the design thickness of pavement structures, which is the basis for the current AASHTO (American Association of State Highway and Transportation Officials) pavement design procedure. The design thickness was based on limiting the loss of serviceability during the intended design life of the pavement structure. This level of loss of serviceability of flexible pavements was related to the amount of cracking and patching of the asphalt concrete surface, the amount of profile variance (roughness), and the depth of the ruts formed in the wheel track. The current subgrade failure criteria, used in mechanistic design for flexible pavements, were also developed from the results from the AASHO Road Test.

AASHO test design

The upper 910 mm of the subgrade soil in the AASHO Road Test was classified as an A-6, having a Group Index ranging between 9 and 13. On average the soil was compacted at a dry density of 1815 kg/m^3 (97.7% of the maximum dry density) and a moisture content of 16%, which is slightly wetter than optimum. The properties of the subgrade soil are provided in Table 1.

The subbase material used in the AASHO Road Test was an uncrushed natural sand gravel and was constructed with a mean dry density of 1634 kg/m^3 and a moisture content of 6.2%. Two materials, a crushed dolomite limestone and an uncrushed gravel, were tested as base course materials in this study. The mean constructed dry density and moisture content of the crushed dolomite were 1634 kg/m^3 and 5.8%, respectively. The gravel base was an uncrushed gravel. Additional properties of the base and subbase layer materials are given in Table 2.

Six traffic test loops were constructed for the flexible pavement experiments. The tangent sections of each test loop were divided into two lanes, and each lane

Table 1. Characteristics of the subgrade soil used in the AASHO Road Test.

Classification (AASHTO M-145) (AASHTO 1990)	A-6
Average values, borrow pit samples	
Max dry density (AASHO T-99-49) (kg/m^3)	1858
Optimum moisture content (%)	15
Liquid limit	29
Plasticity index	13
Grain size finer than (%):	
No. 200	81
0.02 mm	63
0.005 mm	42
Specific gravity	2.71
Average of construction tests:	
Density (% max. dry density)	97.7
Moisture content (%)	16
Constructed embankment tests	
Laboratory CBR, soaked	2–4
Field in-place CBR, spring	2–4
Modulus of subgrade reaction, k (MN/m^3)	12

Table 2. Characteristics of the base and subbase materials used in the AASHO Road Test.

Item	Subbase	Crushed stone base	Uncrushed gravel base
Aggregate gradation, % passing			
38.1 mm sieve	–	100	100
25.4 mm sieve	100	90	98
19.1 mm sieve	96	80	–
12.7 mm sieve	90	68	74
No. 4 sieve	71	50	49
No. 40 sieve	25	21	23
No. 200 sieve	7	11	9
Plasticity index, minus No. 40 material	–	–	3.5
Maximum dry density (kg/m^3)	2210	2227	2243
Field density (% max. dry density)	102	104	102

was loaded at a specified level applied on single or tandem axles. The exception was Loop 1, where no loads were applied. In addition to loading, the other variable was the thickness of the different layers. The test speed was 56 km/hr, and 1,114,000 axle loads were applied over a 25-month period, which included two spring–thaw periods. The traffic was heavily channeled (i.e. there was no traffic wander).

Early mechanistic theory

In the early 1960s, theoretical pavement design methods were introduced, based on preventing excessive stresses and strains in the pavement structure. For example, Dormon and Metcalf (1965) and Peattie (1965) introduced mechanistic design methods using elastic theory for flexible pavements. Peattie proposed limiting the vertical *stress* at the top of the subgrade, whereas Dormon and Metcalf proposed limiting the vertical *strain* at the top of the subgrade.

Both Peattie and Dormon and Metcalf based their methods on data from the AASHO Road Test. Their stresses and strains were evaluated several years after the conclusion of the test; the AASHO Road Test did not include any direct measurements of either stress or strain in any pavement layer or in the subgrade.

Peattie (1965) considered the vertical stress at the top of the subgrade as critical to the performance of flexible pavements. He found a good correlation between calculated surface deflections and the vertical stress at the top of the subgrade. Using data from 23 sections that had decreased to a Present Serviceability Index (PSI) value of 2.5 during the spring of 1959, Peattie calculated the vertical stress at the top of the subgrade as a function of load applications (Fig. 2). However, the theory of vertical stress criteria never caught on.
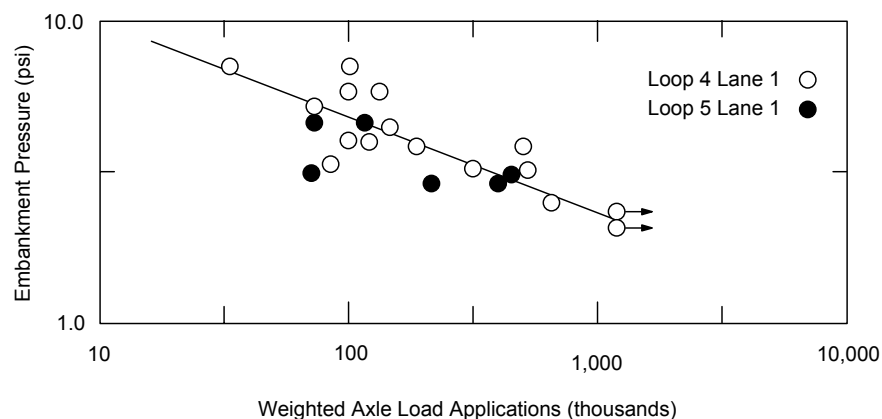
Figure 2. Subgrade stress (embankment pressure) vs. weighted axle load application at PSI = 2.5. (After Peattie 1965.)
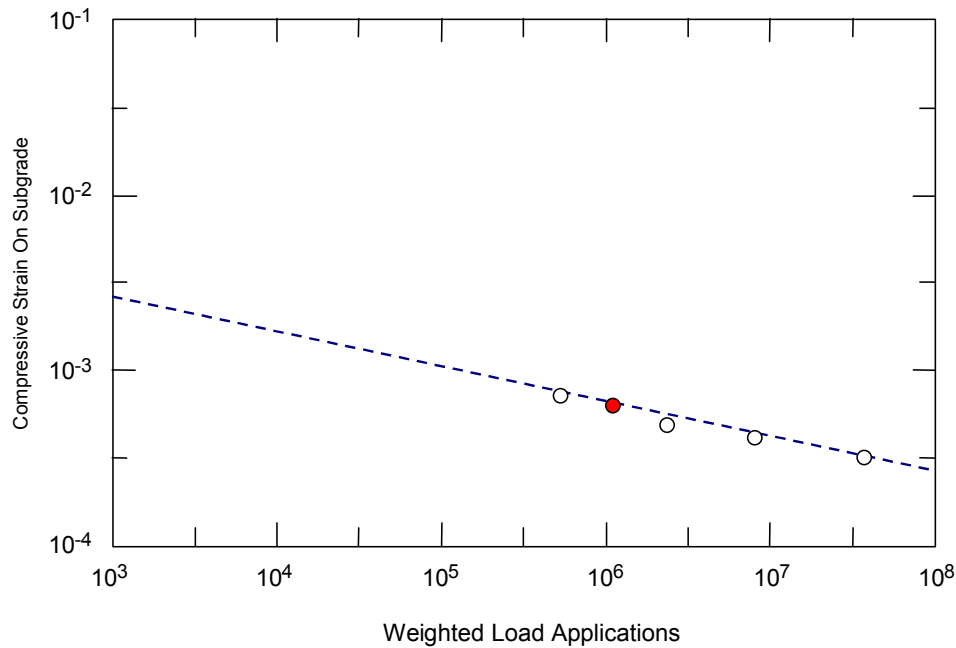
Figure 3. Relation of subgrade compressive strain to number of load applications, 80-kN axle load. (After Dormon and Metcalf 1965.)

Meanwhile, Dormon and Metcalf (1965) developed a similar relationship based on the vertical strain at the top of the subgrade (Fig. 3). The vertical strain was calculated based on a design load of 80 kN. This design load was applied via a contact pressure of 552 kPa and an area of contact, assumed to be a circle, with a radius of 150 mm. The elastic modulus (E in MPa) for the subgrade was based on the relationship using the CBR (California Bearing Ratio) value:

$$E \text{ (MPa)} = 10 \times \text{CBR or } E \text{ (psi)} = 1500 \times \text{CBR.} \tag{1}$$

The modulus for the asphalt layer used in the Dormon and Metcalf analysis was 103 MPa (Brabston et al. 1975). Using calculations from five test sections from the AASHO Road Test, Dormon and Metcalf determined that a compressive strain of 6.5×10^{-4} at the top of the subgrade would result in a surface rut 12.5 mm deep after 1,000,000 repetitions using an 80-kN axle load (filled point in Figure 3). Additional strain calculations from other load levels using a load equivalency factor were used to develop the strain criteria shown in Figure 3.

The subgrade strain criterion was formalized in equation 2:

$$N_d = f_4 \left(\varepsilon_c \right)^{-f_5} \tag{2}$$

where N_d = allowable number of load repetitions to limit permanent deformation

   ε_c = compressive strain on top of the subgrade

f_4 and f_5 = constants determined from road or field performance.

   Huang (1993) tabulated the coefficients (f_4 and f_5) developed by various agencies for the subgrade strain criteria. His findings are presented in Table 3.

Table 3. Subgrade strain criteria used by various agencies. (After Huang 1993.)			
Agency	f_4	f_5	**Rut depth (mm)**
Asphalt Institute	1.365E-9	4.447	12.5
Shell (revised 1985)			
50% reliability	6.15E-7	4.0	
85% reliability	1.94E-7	4.0	
95% reliability	1.05E-7	4.0	
U.K. Transport and Road Research Lab (85% reliability)	6.18E-8	3.95	
Belgian Road Research Center	3.05E-9	4.35	10.2

   The Shell and Asphalt Institute failure criteria shown in Figure 4 are based on the AASHO Road Test. Also shown in Figure 4 are the results from U.S. Army Corps of Engineers Waterways Experiment Station experiments using a full-depth pavement structure over a clay subgrade (Brabston et al. 1975). The design method is based on limiting the vertical strain on top of the subgrade and the horizontal tensile strain at the bottom of the asphalt layer. The selection of the subgrade modulus (E_s) comes either from laboratory tests or indirectly from the CBR value. The modulus of the subgrade when estimated from the CBR was determined using eq 2.

   The Corps of Engineers (COE) limiting subgrade strain criterion is

$$N_d = 10{,}000 \times (a/\varepsilon_v)^b \tag{3}$$

where a = $0.000247 + 0.000245 \log (M_r)$

   b = $0.0658 (M_r)^{0.559}$

and M_r is in psi.
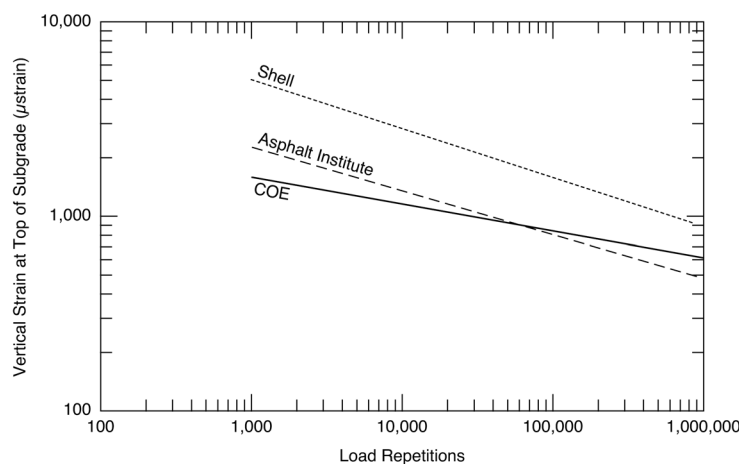
Figure 4. Different subgrade strain failure criteria.

Any limiting subgrade strain criterion developed from the AASHO Road Test needs to be used cautiously. The rut depth measurements taken at the AASHO Road Test sections (155 flexible test sections, of which 143 were loaded) indicated that only 9% of the surface rut occurred because of plastic deformation in the subgrade (the corresponding percentages for the other layers were 32% for the asphalt concrete layer, 14% for the base course, and 45% for the subbase). With failure defined as a PSI of 1.5, it was found that 57% of the flexible pavements failed during the first spring (March, April, or May 1959). An additional 23% failed in the following spring. Overall, 80% of the flexible test sections failed during the spring. The increased failure during the spring period did not allow the "smooth" development of axle load repetitions and damage to the subgrade (Peattie 1965). Furthermore, an elastic parameter—subgrade strain—is being used to predict a plastic phenomenon—rutting—which may not be a rational approach. These limits were recognized at the end of the AASHO Road Test. Because of the limitations of the data from the AASHO Road Test, Peattie (1965) cautioned about the generalized use of the limiting stress or strain criteria to other soil types or environments.

As a result of the work of Dormon and Metcalf (1965), the current design criteria for pavements stipulate that subgrade failure can be predicted by the vertical compressive strain at the subgrade interface. However, the limiting subgrade strain criterion was based exclusively on the A-6 soil at one moisture content, so it may not be applicable for other material types (gravel, sand, silt, or clay) nor for other moisture conditions. For example, practical experience of pavement and geotechnical engineers indicates that silt subgrades rut more easily than gravel and that moisture conditions near saturation are more critical than when the subgrade is less wet.

3   PAVEMENT SUBGRADE PERFORMANCE STUDY

To improve the accuracy of the AASHTO mechanistic–empirical pavement design method, it is important to refine the subgrade performance criteria. This Pavement Subgrade Performance Study is investigating the performance of full-scale pavements involving several types of subgrade soils at several moisture contents. This study will provide new insight into the subgrade rutting phenomenon. The objectives of this Pavement Subgrade Performance Study are to:

- Develop an improved mechanistic subgrade failure criterion (elastic and/or plastic) for new and reconstructed pavements;

- Evaluate the effect of environment on resilient material properties, in particular the effect of moisture content changes over time in the subgrade layers (i.e., "seasonal variability" of pavement materials); and

- Integrate the findings into improved mechanistic–empirical design methodologies for new and reconstructed flexible pavements.

An international group consisting of the U.S. Federal Highway Administration's Turner–Fairbank Highway Research Center (TFHRC), the U.S. Army Corps of Engineers' Cold Regions Research and Engineering Laboratory (CRREL), Cornell University, The Road Directorate of the Danish Road Institute (DRI), and the Technical Research Center of Finland's Road, Traffic and Geotechnical Laboratory (VTT) was formed to conduct this research program. CRREL is the lead research agency and will provide overall project coordination.

In addition to the data generated from CRREL, data from ongoing pavement performance research conducted by the Minnesota Department of Transportation (MN/Road) and by the VTT Road, Traffic and Geotechnical Laboratory of Finland (TPPT study) will be used to verify the mathematical models that will be developed.

This report presents the portion of the work conducted at CRREL. Included in this report are descriptions of the objectives of the study and the techniques and instrumentation selected for use. Subsequent reports will detail the construction of each subgrade soil test and present results and analysis of the data.

4   TEST PROGRAM

The CRREL project plan consists of testing four full-scale pavements using an accelerated load cart. The four materials used as the subgrade were chosen from a range of AASHTO A-2-4 to A-7-6 classifications; the soils are A-2-4, A-4, A-6, and A-7-6. Each subgrade soil is being tested at three moisture levels.

Twelve full-scale test pavements (four soils at three moisture levels) are being constructed in CRREL's Frost Effects Research Facility (FERF) in Hanover, New Hampshire. Each test section is approximately 23 m long, 6.4 m wide, and 3 m deep. Six separate test areas can be tested on each test section, using the load cart at different load levels. To assure uniform moisture content within the test section, total reconstruction of the test sections is required.

The test pavements are being trafficked using an accelerated loading device developed and manufactured by the South African Council for Scientific and Industrial Research (CSIR). The Dynatest/CSIR Mark IV Heavy Vehicle Simulator (HVS) allows for the testing of pavements, which are either built for experimentation or are currently in service.

For this study the test section being loaded is considered to have failed when the surface rut depth reaches a minimum of 12.5 mm. This depth is the same criterion that the Asphalt Institute used for the AASHO Road Test analysis.

The data being collected are:

- Air temperature
- Asphalt surface temperature
- Subgrade temperature
- Subsurface moisture content
- Negative pore water pressure
- Subgrade response in the X, Y, and Z directions, specifically stress, strain, displacement, and surface permanent deformation
- Vertical displacement with respect to a reference datum plane.

5   SOIL SELECTION

Soils selected for this project reflect the common subgrade materials found throughout the U.S. Shown in the generalized soil map (Fig. 5) are nine soil types that are prevalent to the U.S., of which three soils appear to be predominant: residual soils, glacial soils, and coastal plain soils. Residual soils are prevalent in the interior and are generally sandy, highly plastic soils. According to the AASHTO Subgrade Classification System, residual soils are typically classified in the A-2 category (AASHTO Designation: M 145-87). The glacial soils found in the northern states can be classified as either gravel (A-1), sand (A-2), silts (A-5), or silty clays (A-6). The coastal soils along the eastern seaboard and in the gulf area are largely sands and gravel. Note, however, that within this region are extensive areas of highly plastic clays (A-7).

Residual Soils
Filled Valleys and Outwash
Coastal Plain Soils
Alluvium
Glacial Soils
Lacustrine Soils
Loess
Clay and Organic Soils
No-Soil Areas
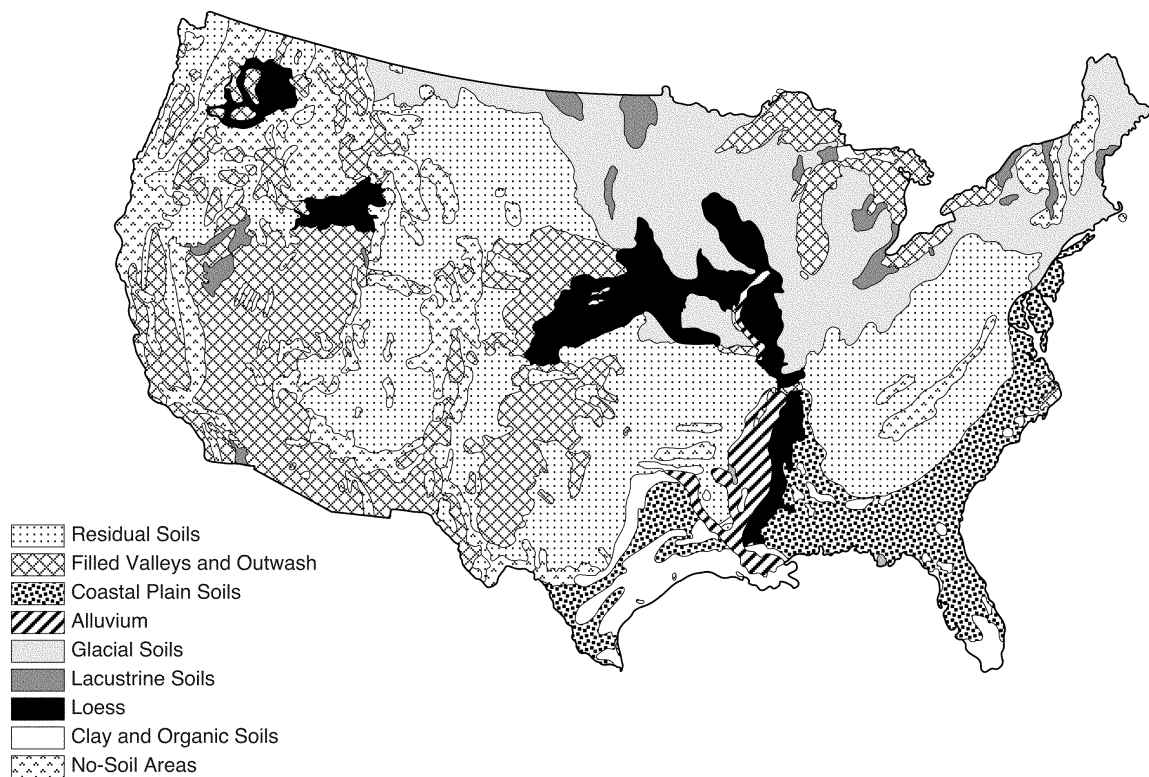
Figure 5. Generalized soils of the United States. (After Yoder and Witczak 1972.)

Table 4. Properties of subgrade test soils.							
Classification			**Atterberg Limits**			**Proctor compaction**	
AASHTO	**Unified Soil Classification System**	**% passing no. 200**	**Liquid Limit**	**Plasticity Index**	**Specific gravity**	**Optimum moisture**	**Maximum density (kg/m³)**
A-2-4	SM	29.9	30	3	2.72	10.0	1950
A-4	ML	84.7	28	8	2.73	16.5	1825
A-6	CL	87.1	33	15	2.79	16.1	1770
A-7-6	CH	84.2	57	37	2.80	22.6	1535

The four subgrade soils selected for testing in the FERF range from A-2-4 to A-7-6 (Table 4). The A-1 material is not being tested because the expected amount of rutting from these subgrades is negligible compared with the other materials.

The initial search for soil was limited to the immediate area around CRREL, particularly areas near the I-89 and I-91 Interstate corridors, for easy transportation. Twenty soils were tested from ten sources. The estimated amount of soil needed for building the test sections in the FERF was approximately 60 m³. Both the A-2-4 and A-4 soils were found locally. The A-2-4 soil was obtained from a local gravel pit in West Lebanon, New Hampshire. To increase the plasticity of the A-2-4 soil, it was blended with some A-4 soil but in a manner so as to maintain the A-2-4 characteristics. The second test soil, the A-4 soil, was obtained from a local excavation site in Hanover, New Hampshire. The remaining test soils, the A-6 and A-7-6 soils, were located in St. Albans and Burlington, Vermont, respectively. The soils were excavated at the various sites and delivered to CRREL, where they are stockpiled.

Characterization of the selected materials falls into two categories. Standard tests were used to define index properties such as density, plasticity, and gradation. Special tests, such as resilient modulus and shear, were used to define the mechanical properties of the soil. These tests were done at Cornell University and the University of Maryland. The results will be presented in future reports. For initial classification testing, site visits were made to the sources, and samples were collected for soil classification. After the soils were delivered to CRREL, samples were taken from several locations in each stockpile, and classification tests were performed again. The standard soil tests described in the following AASHTO publications were performed:

- *Particle Size Analysis of Soils* (T 88-90) (AASHTO 1990a)
- *Determining the Liquid Limit of Soils* (T 89-90) (AASHTO 1990b)

- *Determining the Plastic Limit and Plasticity Index of Soils* (T 90-87) (AASHTO 1990c)

- *Specific Gravity of Soils* (T 100-90) (AASHTO 1990d)

- *Laboratory Determination of Moisture Content of Soils* (T 265-86) (AASHTO 1990e)

- *The Moisture-Density Relations of Soils Using a 5.5 lb (2.5 kg) Rammer and a 12 in. (305 mm) Drop* (T 99-90) (AASHTO 1990f)

- *The California Bearing Ratio at Standard Proctor Density* (T 193-81) (AASHTO 1990g).

The gradations for the four subgrade soils are shown in Figure 6. The results from the Proctor tests are presented in Figure 7. Note for the A-2-4 soil (Fig. 7a), two sets of results are presented, because a second test was run to better define the curve from the first test. Also, the tests for the A-2-4 soil were conducted on material from which anything larger than 3/4 in. had been removed. The CBR results are presented in Figure 8. CBR testing was not conducted on the A-2-4 material because of the large stones in the gradation, which would have made the results too variable.
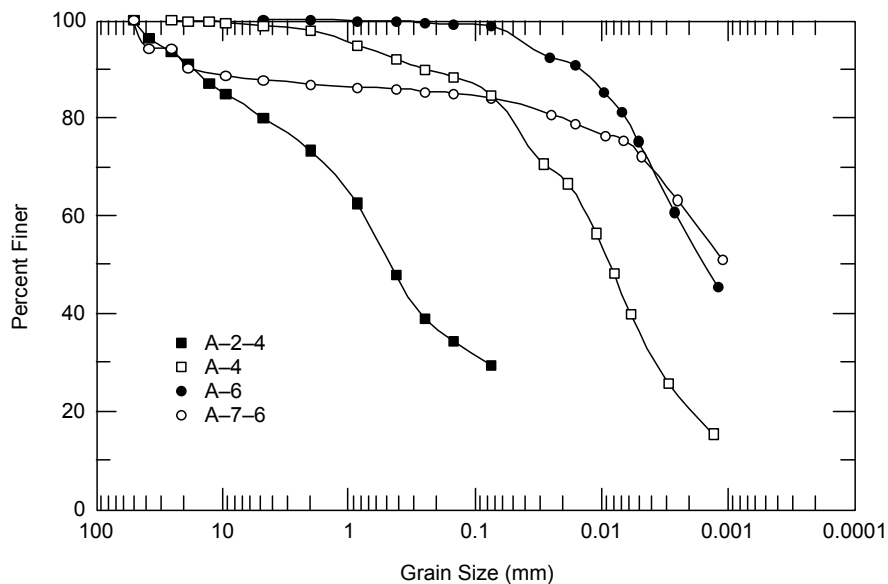
Figure 6. Grain size distribution of test soils.
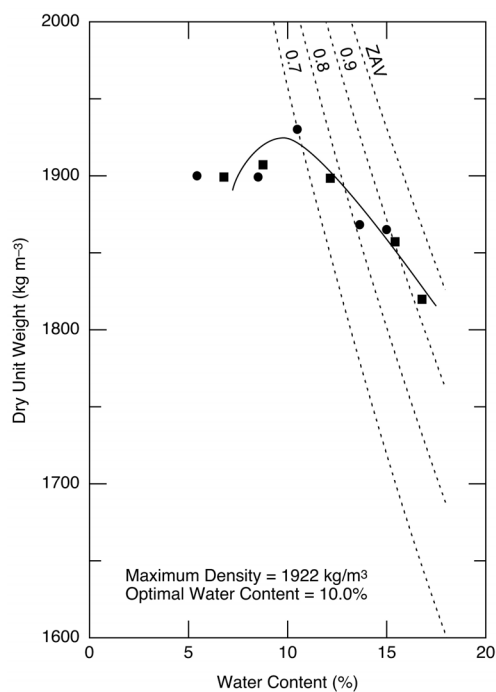
a. A-2-4 soil.
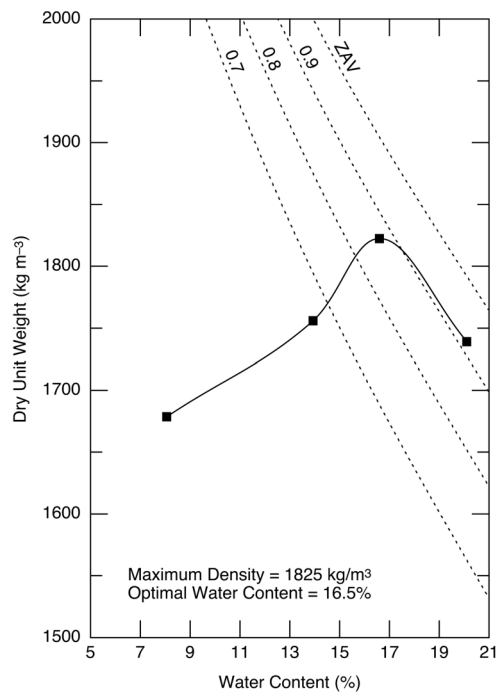
b. A-4 soil.
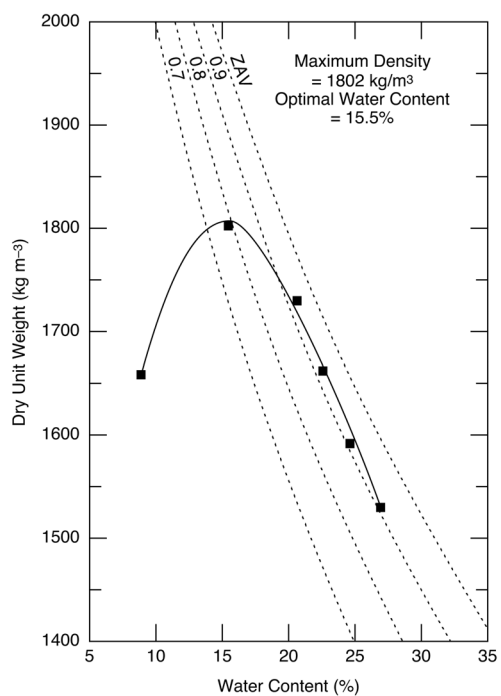
c. A-6 soil.
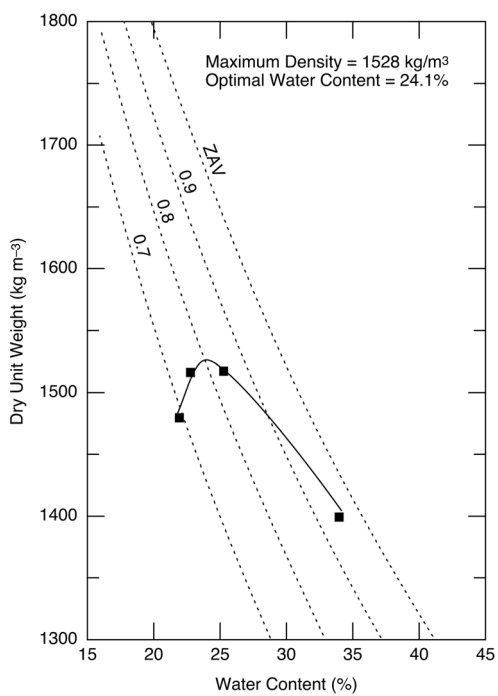
d. A-7-6 soil.

Figure 7. Standard Proctor results for the test soils.
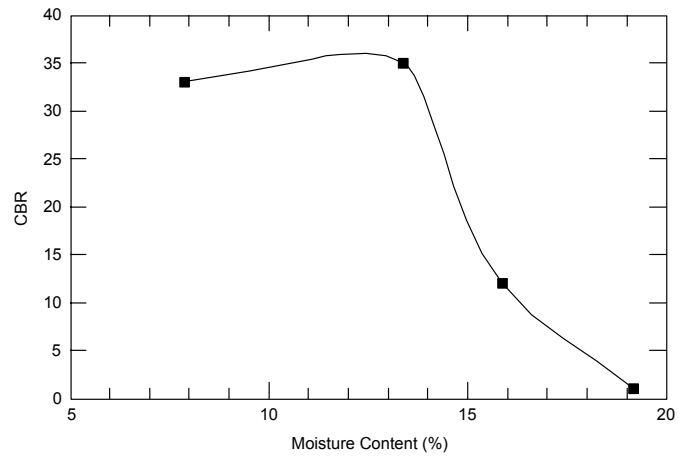
a. A-4 soil.
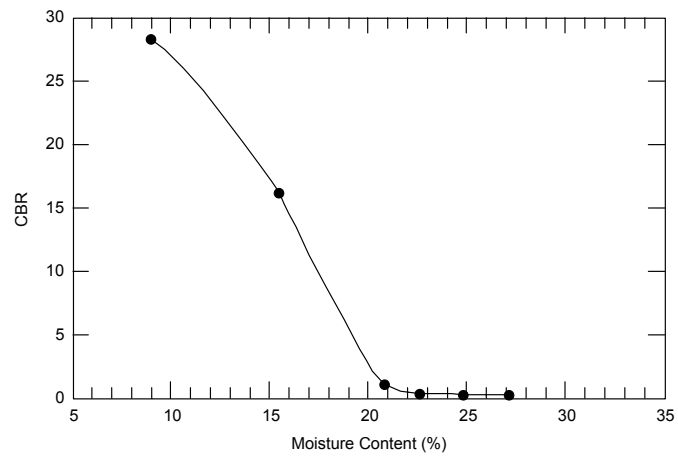
b. A-6 soil.
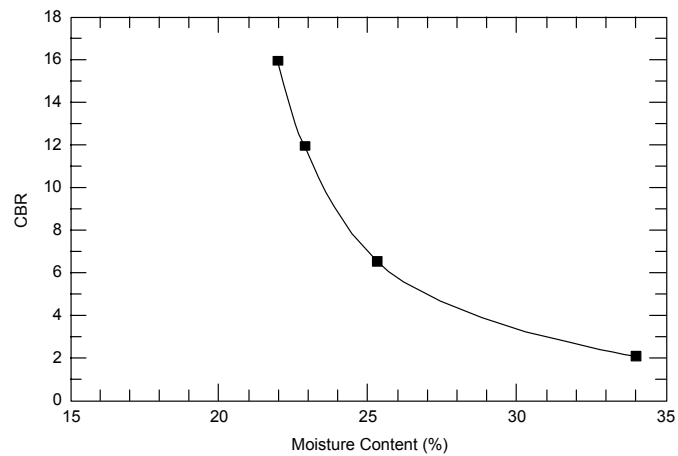
c. A-7-6 soil.

Figure 8. CBR test results for the test soils.

6   DESCRIPTION OF FROST EFFECTS RESEARCH FACILITY

The FERF, where all the construction and testing is being conducted, is a 2700-m^2 environmentally controlled building. The overall facility is 56 m long by 31 m wide (Fig. 9).

Within the facility are 12 test cells, which are 6.5 m wide. Eight of the cells are 7.6 m long and 2.5 m deep. The remaining four cells are 11.3 m long and 3.7 m deep. They can be used individually for smaller experiments or combined in a variety of ways to accommodate larger projects. The cells can be made impermeable to simulate the raising and lowering of the water table.

The ambient air temperature within the facility can be controlled from –3.9° to +24°C with a 2°C tolerance. The temperature in the test cell can be further reduced to –37°C or increased to 49°C using surface panels.

Figure 9. Frost Effects Research Facility (FERF).

Construction of test sections

The test program consists of constructing twelve pavement test sections in the north end of the FERF. An area 42 m long by 16 m wide was made available for this project (Fig. 10). Prior to construction of the test sections, two modifications were made to the test area. A support pad for the HVS was constructed on the south side of the test area (Fig. 10). The pad (4 m long by 16 m wide) was constructed with crushed gravel and capped with a 125-mm-thick concrete slab. The second modification was the placement of a longitudinal wall to divide the
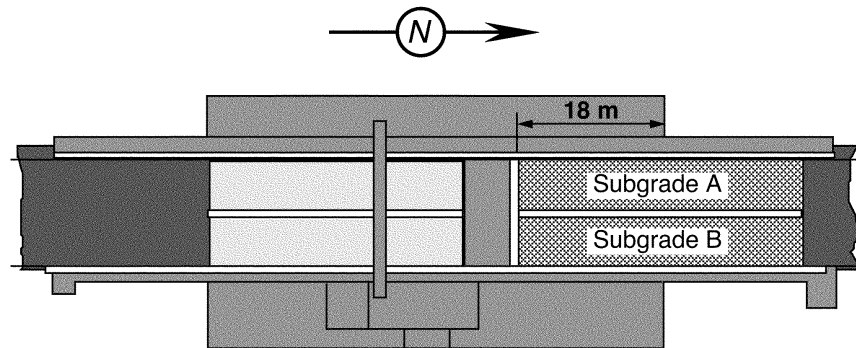
Figure 10. Plan view of the location of the test sections in the FERF.
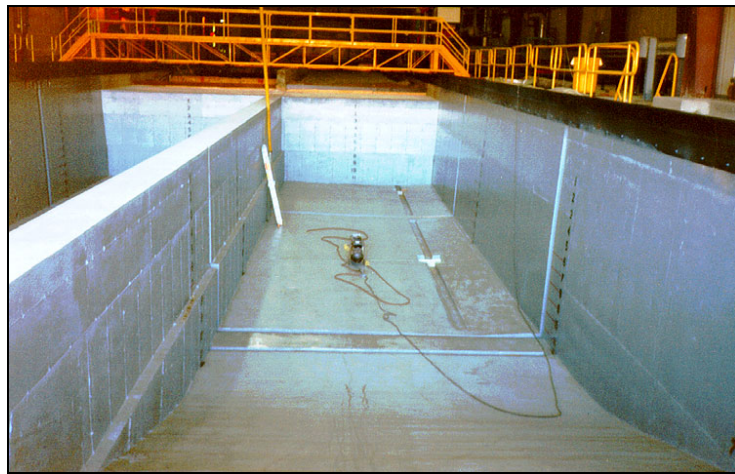
Figure 11. Longitudinal wall separating the test basins.

area into two 42-m-long by 6.4-m-wide areas (Fig. 11). The test area is 23 m long by 6.4 m wide, with a depth of 3 m. To minimize the effect of the ramp, the actual test area is confined to the southern 20-m by 6.4-m area of each test section (Fig. 12). The subgrade materials tested were the A-2-4 in the east section and the A-4 in the west section.

To achieve uniform moisture conditions at three different levels, the subgrade will be reconstructed three times. The experimental design is to construct, for each subgrade soil, one test section at or near optimum moisture and two repetitions of the same material with higher moisture contents. However, existing construction techniques will determine the maximum moisture content of the test section. An individual test area in the FERF is 6.1 m long by 1 m wide. Six test areas are being tested in each test section. The center-to-center distance between
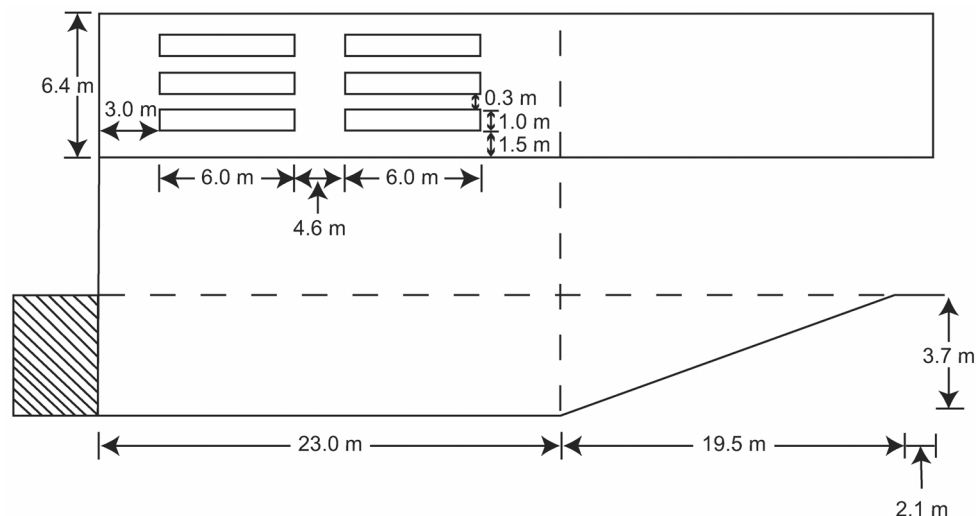
Figure 12. Location of the test area in the FERF.

the test areas is approximately 1.3 m (Fig. 12). This allows us to load the pavement to three failure strain (load) levels and still have three remaining areas to either replicate the first set of tests or increase the number of failure levels. Therefore, the total number of accelerated load tests for this project will be 72.

The initial thicknesses of the test section layers were based on theoretical multi-layered analysis (Hildebrand 1994). The resulting initial thicknesses were 25 mm of asphalt concrete with 152 mm of base course over the subgrade. The results from the Danish Road Institute (DRI) (1997) test sections using the Road Testing Machine (RTM) were used to modify the initial cross sections from the theoretical analysis. Testing at DRI showed that most failure occurred in the base course material. To minimize this in the FERF, the asphalt and base course layers were increased. Based on the results from the RTM test sections, the cross section was changed to 76 mm of asphalt concrete and 229 mm of crushed base over 3.0 m of test subgrade soil (Fig. 13). In addition the base course specification was changed to 100% crushed.

Influence of FERF test section walls

A finite element study using ABAQUS was conducted on the FERF test section to study the effects of the support pad and side walls surrounding the test area (Fig. 10) on the stress and strain state in the test section under a moving tire load. In addition, a corollary study was conducted to determine the minimum distance the test windows could be from the wall without affecting the results, as well as the minimum distance between the test windows.
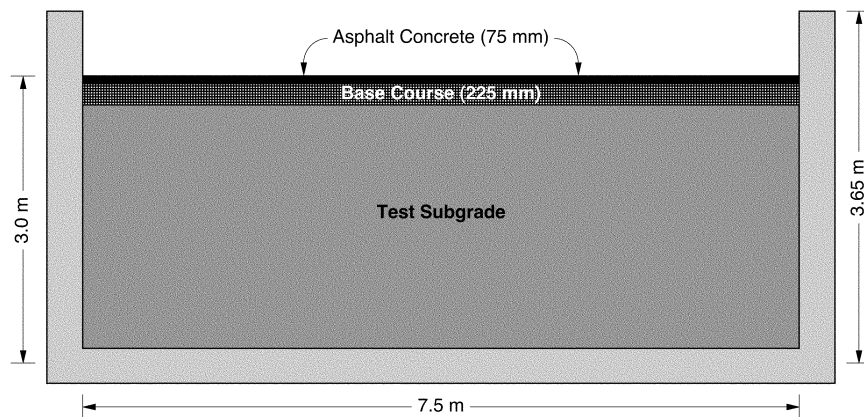
Figure 13. Cross section of the test sections in the FERF.
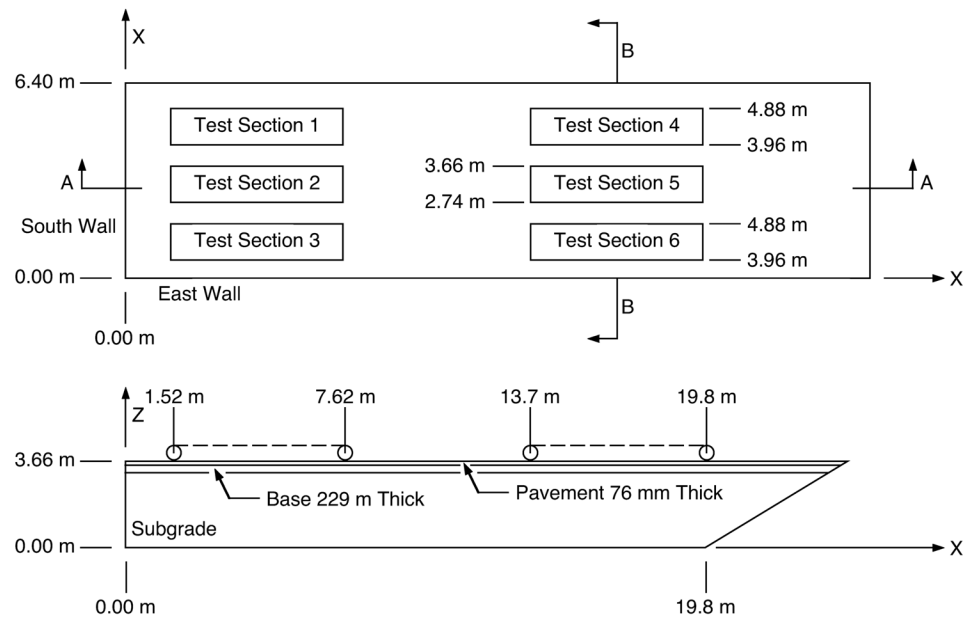
Figure 14. FERF test area used in the analysis.

A schematic of the FERF test area as used in this analysis is shown in Figure 14. The test area is filled with a subgrade material to a depth of 3.0 m and is covered by a base material that is 229 mm thick. This is all paved over with a 76-mm layer of pavement. The test sections in Figure 14 are the patches of the pavement where the accelerated load tests are being conducted. The orientation of the tire travel is along the long dimension of the test section. Each test section is 0.92 m wide and 6.1 m long. They lie 1.52 m from the walls and are spaced

30.5 cm apart. The tire load is applied by a set of dual tires inflated at 620 kPa with a nominal load applied at the axle. For all of the finite element models described below, the load applied at the axle was 80 kN; the resulting contact patch for an individual tire under this applied load is 29.2 cm in the longitudinal or X direction and 22.2 cm in the transverse or Y direction. Note that this analysis was conducted after the construction of the first two test sections. In the first two test sections, test windows 1, 2, and 3 were located 1.52 m from the support pad (south wall). Windows 4, 5, and 6 were located 4.5 m from the edge of the windows 1, 2, and 3.

Three two-dimensional static models were constructed. The first model (the control model) was a simulated infinite medium used to determine the stress distribution in the absence of walls. The model simulates a continuum 30.5 m wide and 30.5 m deep, with the base and pavement comprising the top 305 mm of the model. The tire load is applied in the center of the model. Because of symmetry, only half of the continuum was modeled (Fig. 15). Two load cases were applied. The first case simulated the tire traveling in the plane of the model, as depicted in Figure 15 (side view). The second case simulated the tire traveling perpendicular to the plane of the model (end view).
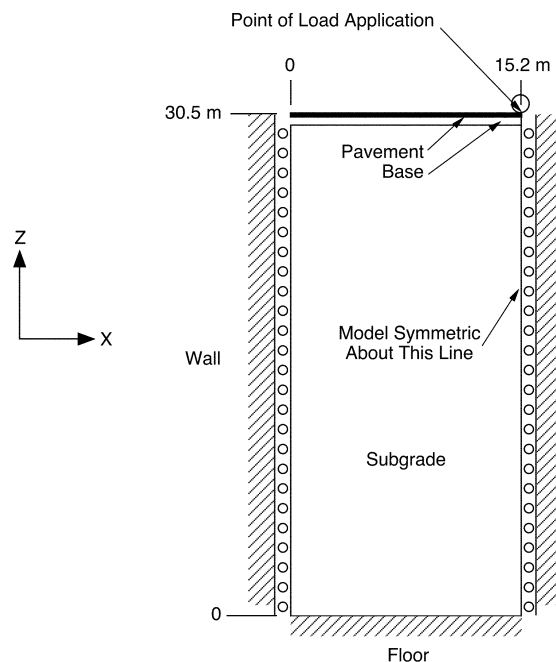
Figure 15. Finite element model geometry for the control section.
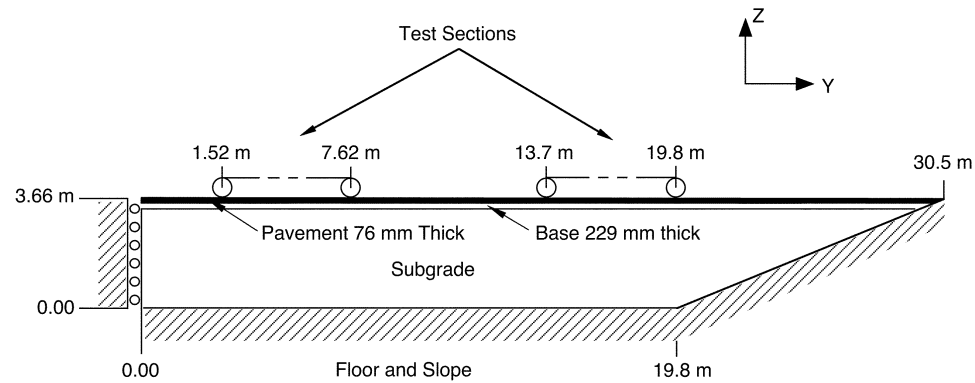
Figure 16. Finite element model geometry for the longitudinal (side) section.
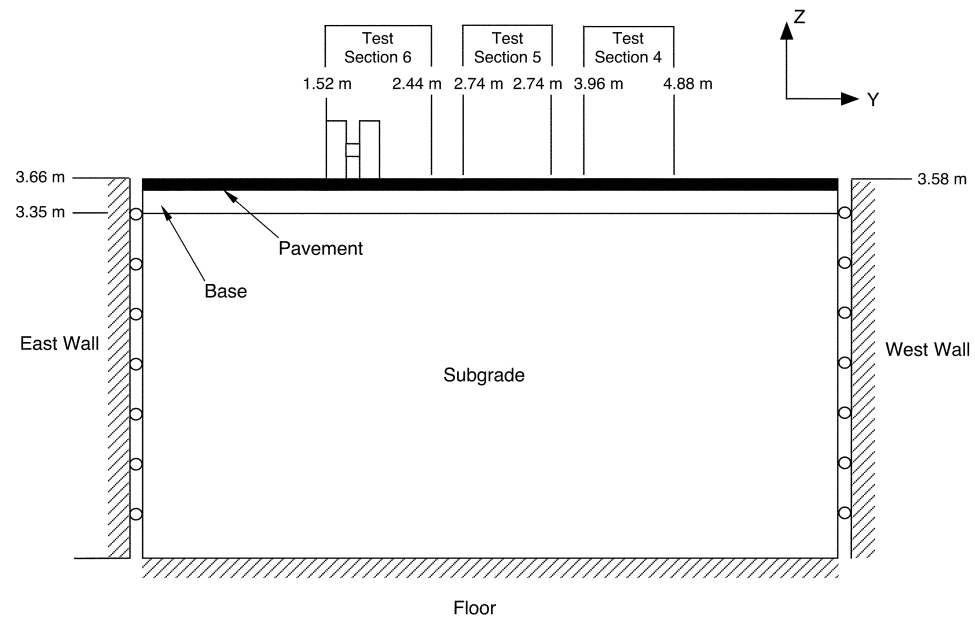
Figure 17. Finite element model geometry for the transverse (end) section.

The second model was the side view of the test area (section A-A, Fig. 14) and is depicted in Figure 16. The load was statically applied at 30.5-cm increments across the entire length of both test sections. This allowed the study of changes in the stress distribution as the load was moved away from the south wall and variations in the stress as the tire approached the sloped region on the north side.

The third model (Fig. 17) was an end view of the test area (section B-B, Fig. 14). During actual testing the tire was incrementally moved from one edge of the

test section to the other through successive passes of the tire. In this model only three load cases were modeled to capture this movement of the load. In the first case the tires were riding on the east edge of test section 6, in the second case the tire was riding on the west edge of test section 6, and in the last case the tire load was centered in test section 5.

Linear elastic constitutive models were used for all of the materials modeled. The material properties for the pavement, base, and subgrade are given in Table 5. For all of the models, two-dimensional plane strain quadrilateral elements were used.

Table 5. Material properties used for the finite element analysis.

Material	Elastic Modulus (MPa)	Poisson's Ratio
Pavement	3100	0.3
Base	410	0.4
Subgrade	83	0.4

To make the load fit on the 7.6-cm-square mesh of the finite element grid, the contact area of the load differed slightly from the actual tire contact area. Table 6 shows the difference between the actual and model contact areas for the side and end views of the tire.

Table 6. Comparison of the modeled and actual contact patches.

	Side view	End view
Actual	29.2 cm	22.2 cm separated by 11.4 cm
Model	30.5 cm	22.9 cm separated by 7.6 cm

Strain sensors were installed in each test section (a complete description of the instrumentation is presented later in this report). The measurements obtained from these sensors were used to validate the finite element model results. Viewed from the end (section B-B, Fig. 14), the array of seven sensors was located at the centerline of each test section. The arrays extended from 152 mm below the pavement surface to 1.22 m deep. The sensors were spaced 152 mm apart in the array. The measurements were compared to the strain field obtained from the end model with the load placed in the center of test section 6.

Effects of confinement on the stress distribution

The stress field obtained in the control model was used to normalize the stress fields obtained from the side- and end-view models. Figure 18 shows the normalized stresses for the side model, and Figure 19 shows the normalized stresses for the end model. These plots were obtained by normalizing each load case for the side and end models and then creating a composite normalized stress map.
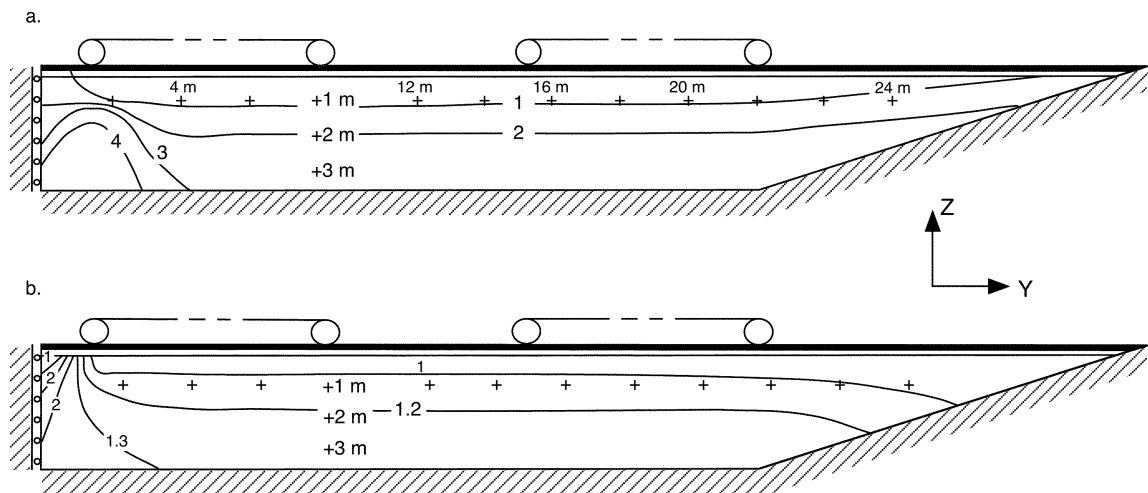
Figure 18. Normalized stress field for side (longitudinal) model: (a) horizontal stresses, (b) vertical stresses.
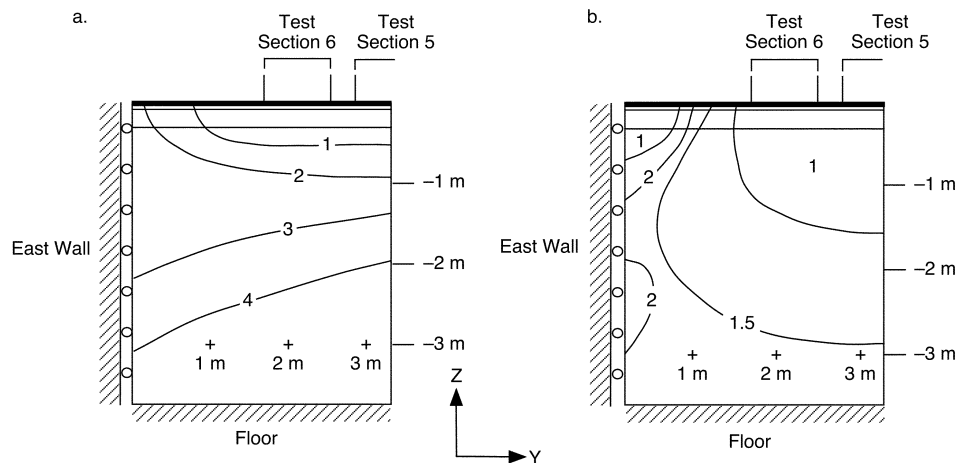
Figure 19. Normalized stress field for end (transverse) model: (a) horizontal stresses, (b) vertical stresses.

These stress maps highlight how the walls and floor affect the stress (and strain) distribution in the test section and show that the stresses are significantly higher because of the confinement of the walls and floor. The region that gives a one-to-one stress correspondence between the control and side models for both the horizontal and vertical stress components extends from the pavement surface to about 1 m deep (slightly deeper for horizontal stresses and slightly shallower for vertical stresses, Fig. 18). However, the horizontal stresses rise rapidly below this unaffected region, and at a depth of 2 m the predicted stress in the test section is twice that predicted for the unconfined control model. The vertical stress component does not rise so rapidly, and at a depth of 2 m the stress level is 20% higher than the unconfined stress. Near the wall the stress is further elevated (Fig. 18). For the horizontal stresses the effects of the south wall extend about 1.5 m into the test section, yet for vertical stresses the effects of the wall do not extend into the test section more than a few centimeters. Figure 18 also shows that the slope on the north end of the test section has little impact on the stress field near the test sections.

Figure 19a shows a similar result for the end view, though for the horizontal stress the area unaffected by the walls and floor extends to only 0.5 m, and at a depth of 1 m the stress is twice that of the control model. Again, the vertical stress is not affected as much by confinement, with the unaffected region extending to about 1.5 m (Fig. 19b).

The geometries of the unaffected regions for each of the tensor directions are summarized in Table 7. The distance from the wall to the edge of the unaffected region is the minimum allowable distance that the test sections should be placed from the wall.

Table 7. Geometry of the region of the FERF test area that is unaffected by confinement imposed by the walls and floor.			
Tensor direction	**Depth (m)**	**Distance from south wall (m)**	**Distance from east/west wall (m)**
X	1.2	1.5	N/A
Y	0.5	N/A	1.2
Z	1.3	1.5	1.5

Minimum spacing between test sections

The minimum allowable distance between adjacent test sections depends on the extent of damage in the material surrounding a single test section. For this

analysis we defined the damage envelope as the area in which the stress in the material equaled or exceeded the applied contact pressure. Table 8 summarizes the geometry of the damage envelope determined from the finite element analysis for the three tensor directions. This table shows that the limiting case is the Y direction stress, which has a damage envelope that extends 120 mm from the edge of the tire contact patch. This needs to be doubled to obtain the minimum distance between adjacent test sections.

Table 8. Geometry of the area bounded by stresses equal to or greater than the contact pressure.

Tensor direction	Depth below tire/ pavement interface (cm)	Distance from edge of tire contact area (cm)
X	4.0	7.0
Y	8.0	12.0
Z	19.0	0.0

Comparison of finite element model with test data

A set of measured strain data was obtained during the test that had a 27-kN load applied at the axle, so this was used to compare with the model results. Since the modeled load (80 kN) was higher than any of the applied loads used in the actual tests, direct comparison of the model results and the test data could not be made. However, since a linear elastic constitutive model was used, the applied load scales the computed strain (or stress) obtained from the finite element model. Therefore, comparison of the model results to these test data could be accomplished by reducing the computed strains by a factor of 27/80 = 1/3. For the purposes of this comparison, we considered any differences in tire contact area between the model and test to have a negligible effect on the strain field.

Figure 20 compares the measured strain in the test section to the computed strain using the finite element model. In both the test and the model, the load was applied at the center of test section 6. Figure 20 gives the resulting strain directly under the point of load application (test section 6) and in the adjacent test sections 4 and 5. The model shows generally good agreement with the measured test results, with the same overall trends. In the Y direction the sensor at 0.3 m failed, so no data are shown for that depth; nevertheless, the measured and computed strains at 0.15 m are in agreement. However, in the subgrade the test results show that the model significantly overpredicts the strain. Below the point of load application and at a depth of about 1 m, the measured strain is essentially zero in both the Y and Z directions, yet the model predicts over 800 μstrain in both tensor directions at that depth. The predicted strain in the adjacent test sections is
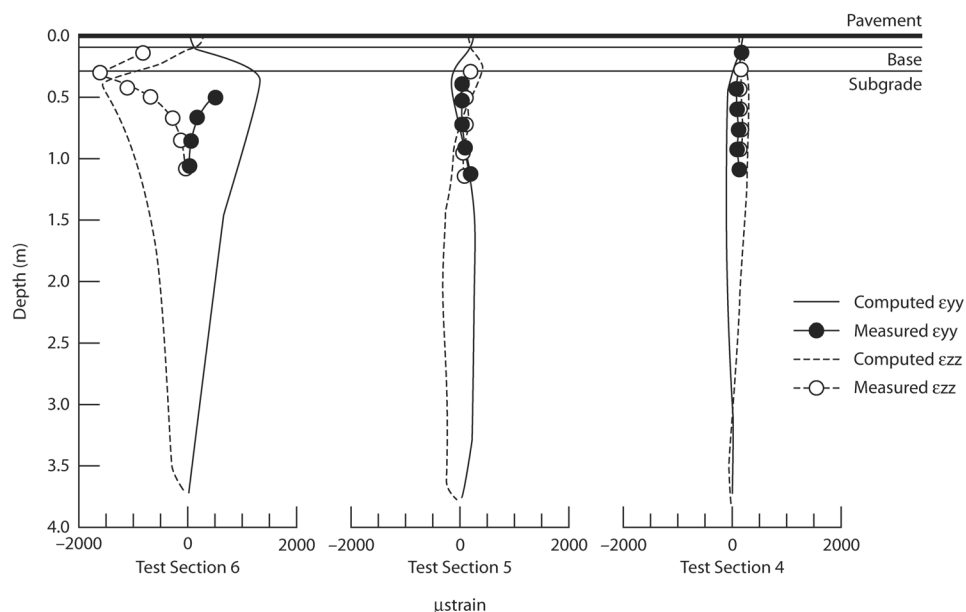
Figure 20. Measured vs. computed strains.

also much higher than the measured strain. These differences suggest that the constitutive model for the subgrade needs to be modified; a higher elastic modulus is necessary for the subgrade if a linear elastic model is used. Despite the shortcomings of the linear elastic model, its results need not be discarded entirely. Since it overpredicts the strain, the conclusions drawn from this model regarding test section spacing and location are inherently conservative.

In summary, the finite element analysis showed that the influences of the walls and floor on the stress field in the FERF test facility dictate that the test sections should not be any closer than 1.5 m from a wall. This analysis also showed that to a depth of 1.2–1.3 m the stresses that act in the X and Z directions are largely unaffected by the presence of the floor. For stresses acting in the Y direction, the depth of this unaffected region extends to only about 0.5 m. Furthermore, the finite element model showed that the slope on the north end of the FERF does not significantly affect the stress field. This study also showed that the minimum spacing between adjacent windows should be no less than 14 cm in the X direction and 24 cm in the Y direction.

Accelerated loading of the test sections

The test sections are being loaded using the Mark IV Heavy Vehicle Simulator (HVS), an accelerated loading system. The load is transferred to the pavement through dual truck tires. The HVS has been used by CSIR, South Africa for

approximately 20 years. The HVS delivered to CRREL (Fig. 21) was a modification of the existing MK III. The modifications included increased speed capability, automatic and manual controls, and an electric motor to drive the test carriage. The HVS is monitored continuously, and it is set to automatically shut down out if a major problem is detected.

Figure 21. Heavy Vehicle Simulator (HVS).

The HVS is approximately 23 m long, 4 m wide, and 4 m high and weighs about 45,000 kg. It can accommodate dual truck tires, a super single truck tire, or a C-141 aircraft tire. The load on the dual and super single can range between 20 and 111 kN. The C-141 tire can be loaded to 200 kN. The loads on the dual or super single can be applied in one or both directions. The length of the test section where the load is applied at constant velocity is 6 m. The load on the dual tires or super single can be applied at a creep rate of up to 13 km/hr. An additional feature of the Mark IV HVS is the ability to program the load distribution on the pavement section. The maximum lateral wander of the test wheel is set at 1.0 m. Table 9 summarizes the features of the HVS Mark IV.

For this project the speed is set at 13 km/hr, and the number of load repetitions on the dual tire in one direction is approximately 700 per hour. The HVS is operated 22 hours per day, 7 days a week. After a meeting of the expert task group for this project, uni-directional trafficking of the test was selected, because highways pavements are subjected to uni-directional roads and there was concern in the group about the effect of bi-directional loading (due to lack of data) on the pavement response and in turn on the subgrade failure criteria. The sections are being subjected to wheel wander over the width of the test windows in increments of 5 cm.

Table 9. Performance information for the Mark IV HVS.	
Wheel load	Typically 20–100 kN (4.5–22.5 kips)
Test wheel	Single, dual, or aircraft
Tire pressure	Typically 560–690 kPa (80–100 psi) on roads; up to 1450 kPa (210 psi) on airfields
Repetitions, per day	Approximately 18,000 (bi-directional)
Trafficked length	Approximately 7 m (approx. 23 ft)
Trafficked width	Variable up to 1.5 m (approx. 5 ft)
Trafficked pattern	Variable

7   CHARACTERIZATION OF THE FERF TEST SECTIONS

As the test sections are built in layers, testing is being conducted to characterize the layers. The lower 2.0 m of subgrade is compacted in 30-cm lifts. The upper 1.0 m of subgrade soil is compacted in lifts of 15 cm. Quality control of the construction is being measured in terms of density, moisture content, elevation, falling weight deflection (FWD), and CBR. The elevation, CBR, density, and moisture are being measured on every consecutive layer (i.e. every 300-mm thickness). The locations of the elevation and Clegg hammer points are shown in Figure 22. The lift thicknesses and locations of instrumentation are determined using rod and level measurements (Fig. 23).
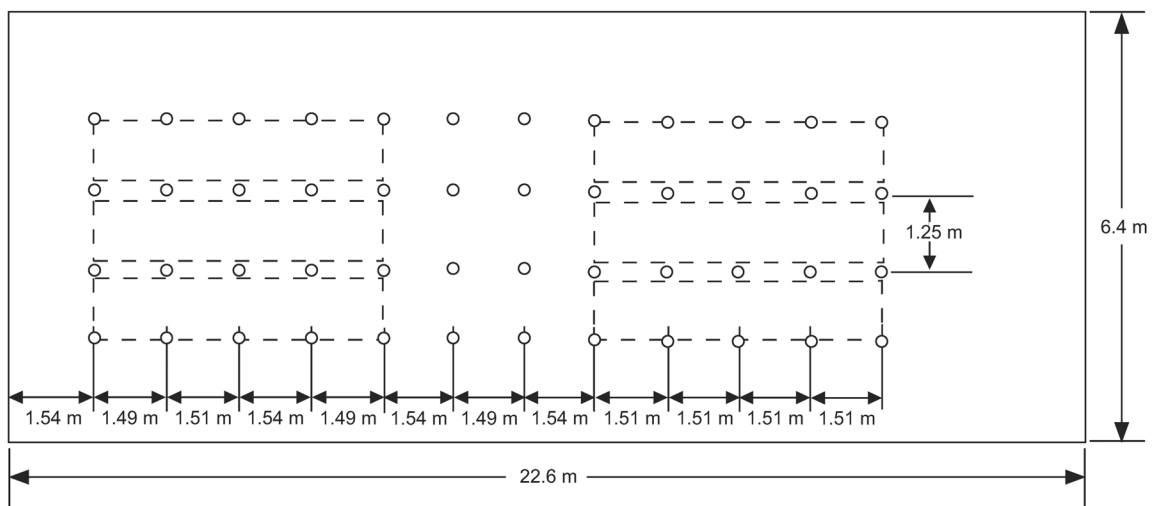
Figure 22. Locations of elevation and Clegg hammer points.

The Clegg hammer is shown in Figure 24. It is essentially a modified AASHTO compaction hammer fitted with a piezoelectric accelerometer. It is used in Canada, Australia, and Europe for compaction control of subgrade, subbase, and base courses. A 4.5-kg hammer is raised to a height of 457 mm inside a guide tube and then dropped. A hand-held meter measures the peak deceleration as the hammer hits the surface. The deceleration is presented as the Clegg impact value (CIV).The CBR of the layers are determined from the relationship CBR (%) = (CIV^2). The Clegg hammer test is a fast, non-destructive tests and provides a good indicator of lift uniformity. A total of 48 elevation and Clegg hammer tests are being conducted on each 300-mm lift.

Figure 23. Rod and level measurements taken on the compacted subgrade lift.

Figure 24. Clegg hammer test.

When possible, FWD measurements are being taken as the subgrade is built (Fig. 25). The geophone sensors are located 0, 203, 300, 600, 900, 1200, and 1800 mm from the center of the loading plate. The plate diameter used on the subgrade is 457 mm. The deflection testing is done using the SHRP protocol of seating loads at the third drop height followed by four drops each at four drop heights, for a total of 16 deflection basins. The locations of the FWD test points are shown in Figure 26. The deflection testing is primarily conducted in the test area. A total of 24 test points are being conducted on each lift. On the surface, FWD testing is conducted before and after completion of the accelerated load tests. Prior to construction of the test sections, FWD measurements are also taken on the concrete slab beneath the subgrade. The deflection data will be used in conjunction with back-calculation techniques such as MODCOMP to determine the stiffness of the concrete layer, the subgrade soil, the base course, and the asphalt layer.

Figure 25. FWD measurements on the subgrade lift.
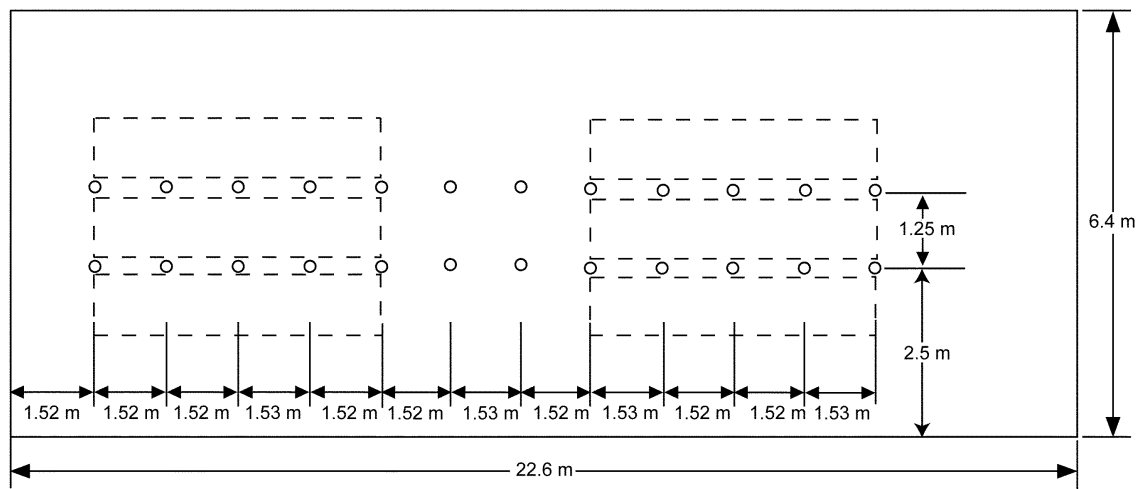
Figure 26. Locations of falling weight deflection (FWD) test points.

In addition to FWD tests, dynamic cone penetrometer (DCP) tests are being made to measure the uniformity of strength of the subgrade. The DCP consists of a 4.5-kg hammer (Fig. 27) that is raised to a height of 584 mm and then dropped on an anvil. The force on the anvil drives the cone into the soil. The number of blows required to drive the cone to each 25-mm increment of depth is noted. The DCP index, which is the amount of penetration per blow, is calculated by dividing the depth of penetration by the number of blows. The DCP index is converted

to CBR using relationships developed by the Corps of Engineers (Webster et al. 1992). DCP tests were conducted next to the FWD test points.

Finally, density and moisture contents are measured using the Troxler nuclear density moisture gage. The locations of the measurements for density and moisture content are shown in Figure 28. A total of 30 moisture density measurements are taken per 300-mm lift.

Instrumentation for measuring temperature, moisture, stress, and strain is being installed during the construction. The type, number, and locations of the sensors are presented in the next section.

Figure 27. Dynamic cone penetration test.
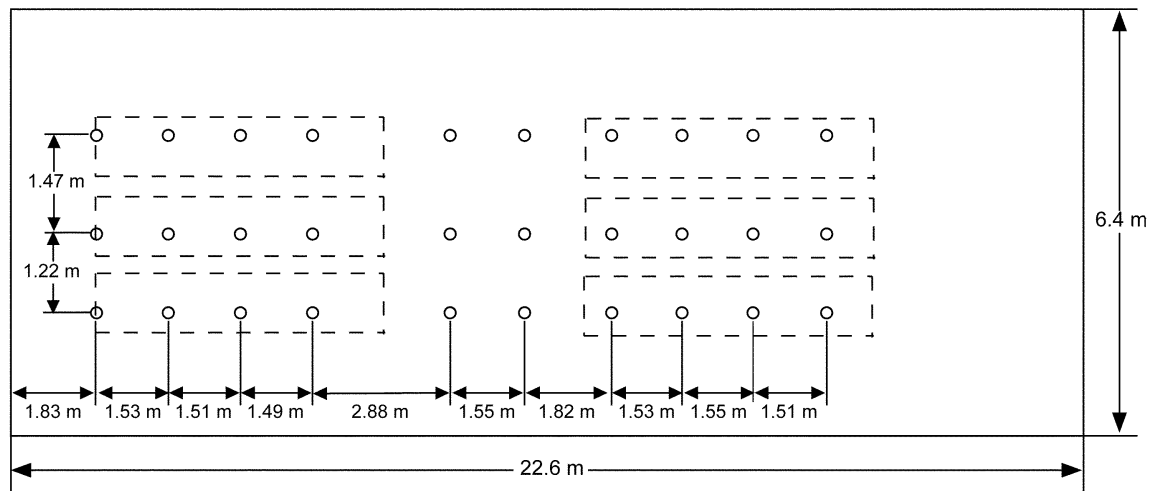
Figure 28. Locations of moisture and density measurement points.

8   INSTRUMENTATION

The data being collected in this study can be divided into two groups: general and load response data (Table 10). The general data group contains information about individual test sections, such as soil type, layer thickness, and test wheel. Included in the general data are the in-situ (temperature, moisture, suction) conditions prior to, during, and at the end of each test.

Table 10. General data collected for each test section.	
General data	**Load response data***
Test section identification	Stress (X,Y,Z)
Subgrade soil type	Strain (X,Y,Z)
Pavement layer thicknesses	Displacement (X,Y,Z)
Position of instruments	Surface permanent deformation:
Time elapsed from construction to first loading	Vertical displacement with
Wheel configuration	respect to a reference datum
Tire type	plane
Wheel load	
Tire pressure	
Wander distribution (specified)	
Falling weight deflections	
In-situ data:	
Air temperature	
Pavement temperature	
Subsurface temperature	
Subsurface moisture content	
Negative pore water pressure (suction)	
*In base and subgrade materials	

Much of the general data are being obtained prior to testing under traffic. However, data such as wheel load, tire pressure, and actual wheel wander are being monitored throughout each test. The second group of data in Table 10 contains the load response data, including the dynamic stress, dynamic and permanent strain, FWD surface deflection, and permanent surface deformation. Surface deflections are measured with the FWD at the beginning and end of each test. Subsurface stresses, strains, and permanent displacements are measured in the vertical and in two perpendicular horizontal directions after 0, 500, 1,000,

2,500, 5,000, 10,000, 25,000, 50,000, 100,000, 200,000, 500,000, 1,000,000, etc. load repetitions.

For ease of querying the database, the test sections are numbered in the seven hundreds. For example, the first test section is identified as 701, the second test section as 702, and so forth. Each of the six windows within the test section is further identified as C1 to C6. For example, a test window in the database could be 701C1 or 702C3, representing test window 1 in test section 701 and window 3 in test section 702, respectively.

Table 11 shows the types of measurements being made in the various pavement layers. It also shows which data are being measured under the wheel path centerline and which are being measured in the vicinity so as to minimize any reinforcing effect of the instrumentation.

Table 11. Measurements in each test section layer.		
	Outside zone influenced by wheel load	**Under wheel path centerline**
Asphalt concrete	Temperature	None
Base course	Temperature Moisture content Negative pore water pressure	Displacement (X,Y,Z)
Subgrade	Temperature Moisture content Negative pore water pressure	Stress (X,Y,Z) Displacement (X,Y,Z)

Instrument types

The following types of instrumentation were installed in the test sections (Table 12).

For temperature measurements, thermocouple strings are used in the surface and subsurface. Air and subsurface temperatures are collected on an hourly basis. Surface temperatures are collected during rut depth and FWD measurements at a depth of 38 mm in the asphalt layer. Subsurface moisture is measured with a Vitel Hydra Probe on an hourly basis. Soil pore pressures (negative and positive) in the subgrade are measured with soil suction devices developed specifically for this project. The temperature, moisture, and pore pressure measurements are collected using a Campbell Scientific datalogger; three dataloggers are in use: the CR7, CR10, and 21X.

Table 12. Type, location, and number of sensors in each FERF test section.

Type of instrumentation	Location	Estimated number per test section*
Soil strain coils	In wheel path	144
Soil stress gages	In wheel path	21
TDR probes	Outside wheel path	6
Soil suction gages	Outside wheel path	6
Temperature probes	Outside wheel path	3
*Note: One test section includes six test windows.		

Stresses in the X, Y, and Z directions in the subgrade are measured using Dynatest soil stress cells. Additional stress measurements in the base and on top of the concrete floor are made with Geokon stress cells. Experimental piezoelectric stress measurement cells are installed in some of the test sections. Strain (X, Y, and Z) measurements are made with inductive coil measurement systems (εmu strain measurement system). Typical planned locations of the different gages are shown in Figure 29.
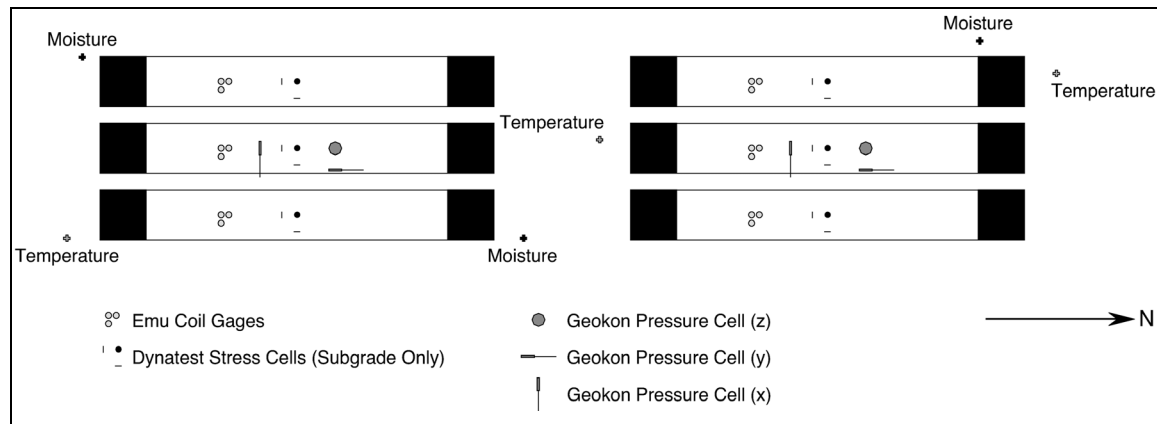
Figure 29. Proposed locations of instrumentation in test section.

For the first two test sections, sensor placement was located using measuring tapes mounted on the center and side walls. The X direction was in the north–south direction, and distances were based on measurements along the walls, with north positive. The distance along the string from the center wall to the side wall represents the Y direction, with west positive and east negative. Sensor placement was marked with a plumb bob and measured with a tape from the string to the sensor for the Z direction. Later, beginning with test section 703, a theodolite was used to locate (X, Y, and Z) sensor placement locations.

Thermocouples

A thermocouple operates on the principle that an electrical potential exists between two different metals placed in contact. At a constant temperature, there is no current flow, as the electromagnetic forces (emf) at the junction are equal and in opposite directions around the electrical circuit. However, if the temperature at one of the junctions changes, its emf is changed and the two junctions are no longer electrically balanced. The current flow or net emf can be measured and calibrated with the temperature at the junction.

The advantages of thermocouples are that they are rugged, easy to read, and inexpensive to fabricate and install. However, their accuracy is generally ±0.5°C, and they require a reference if a single junction is used. They can also pick up electrical noise. The datalogger system being used for this project has reference junctions for the thermocouples and does 60-Hz noise reduction.

The thermocouple strings for subsurface measurements are constructed using 20-gage copper–constantan wire (Fig. 30). Single thermocouples are used for measuring the air and asphalt concrete surface temperatures. Generally, placement of the thermocouple strings in the test sections involves drilling approximately three 25-mm boreholes into the completed subgrade. The strings are always placed in a hole between two test windows and backfilled with the same soil. In the base course layer, a single thermocouple was placed in the middle of the lift as it was being compacted.

Vitel soil moisture sensor

Soil moisture is measured with Vitel soil moisture probes. These probes use a high-frequency (50-MHz) complex dielectric constant measurement for estimating soil moisture and salinity. The dielectric constants of water, soil particles, and air are approximately 80, 4, and 1, respectively. Thus, as a soil is wetted, the dielectric constant increases steadily. Through the use of appropriate calibration curves, the dielectric constant measurement can be related to soil moisture.

The probe has three main structural components: sensing tines, a probe head, and multi-conductor cable (Vitel Inc. 1994). The probe measures moisture, salinity, and temperature. According to the manufacturer, the probe will operate over a temperature range of –10° to + 65°C. The outer three and center tines (Fig. 31) surround the volume of soil from which the probes measure electrical response. The direct-burial multi-conductor cable serves as a conduit for power and data retrieval to and from the probe, respectively. All voltages carried on the cable are d.c. voltages. The probe head contains the electronics to generate the 50-MHz signal and voltages that reflect the soil's electrical properties. The probe
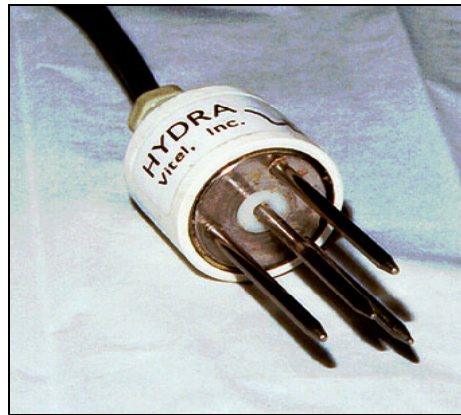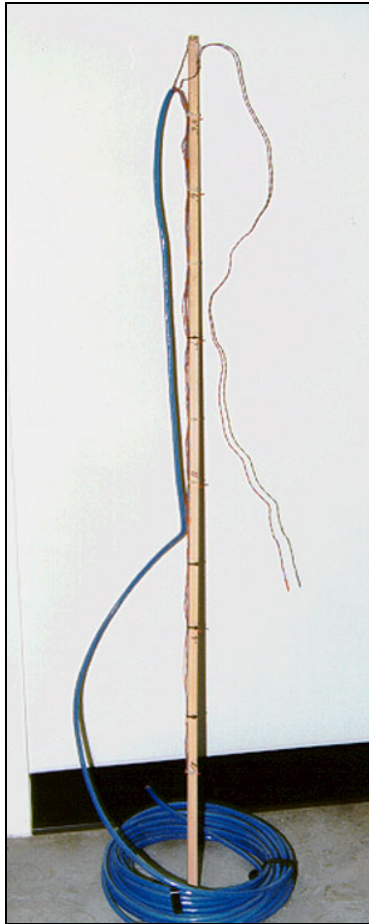
Figure 30. Thermocouple gage.   Figure 31. Vitel Hydra moisture sensor.

also has an embedded thermistor used to determine the in-situ temperature. The output is a set of four voltages, which are processed by proprietary software to convert them into moisture, salinity, and temperature values.

Three equations are available in the software to convert the appropriate voltages into volumetric moisture content. Currently the soils supported in the proprietary software are sands, silts, and clays. For these soils, Vitel claims a 3% accuracy of water content by volume. Greater accuracy can be obtained with specific soil calibration.

The Road Directorate of the Danish Road Institute also used Vitel probes to estimate in-situ moisture contents in the A-4 soil in the Road Test Machine. They found that the moisture measurements from the Vitel probes were generally higher than Troxler nuclear gage measurements. Similar results were found with measurements in the FERF with the A-2-4 subgrade test soil. Therefore, the Vitel

moisture probes were calibrated for the four test soils, and calibration curves and equations developed. The calibration process is discussed below.

Six sensors were installed in each test section placed at intervals of 305 mm vertically staggered between the test windows. The sensors are placed in a rectangular hole (approximately 30 cm long by 15 cm wide by 10 cm deep) in the compacted subgrade layer. The north face of the hole was made as close to vertical as possible. A dummy gage with tines slightly smaller than the actual gage was pushed into the face of the hole. The dummy gage was then removed, and the actual gage was pressed into the tine holes with the cable running along the length of the large hole to the current surface of the subgrade. Upon completion of the installation, the tines were horizontal.

The Vitel moisture probes were calibrated for each of the four soils used in this study. The first step in calibrating the Vitel moisture gages was to ensure that the soil sample was completely dry by oven drying it. Once the soil was dry, a sufficient quantity to fill a container was weighed and placed in a stainless steel mixing bowl. The appropriate quantity of water was added to the sample to obtain the desired volumetric moisture content. The sample was then manually mixed to a uniform consistency, sealed with plastic wrap, and allowed to stand in the bowl overnight to permit the mix to equilibrate.

A 454-g metal container was filled with the prepared sample (Fig. 32). The soil was compacted in layers of approximately 2.54–3.8 cm, using a 5-cm-diameter hand tamper. A Vitel gage was inserted into the sample so that the four metal tines were completely in the soil. Measurements were taken at intervals of 5, 10, 15, and 25 minutes after inserting the probe into the soil using a Campbell Scientific 21x micrologger. Four voltage readings were taken manually and
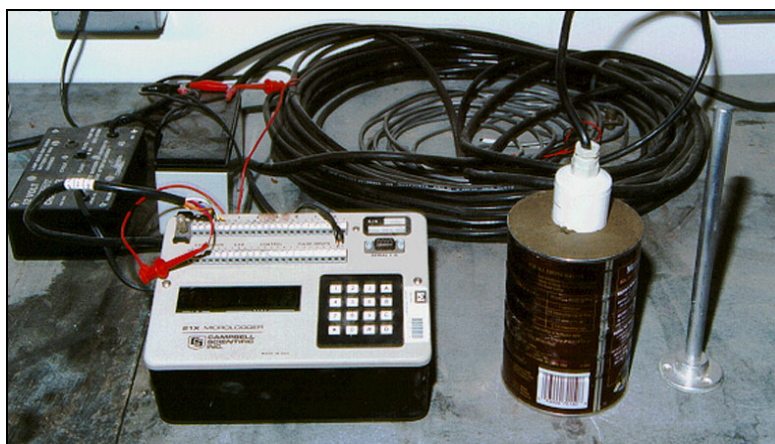
Figure 32. Vitel gage calibration.

recorded. These readings were later inserted into the Vitel proprietary computer program to calculate the volumetric moisture content of the soil. Figure 33 shows the results of the calibration.
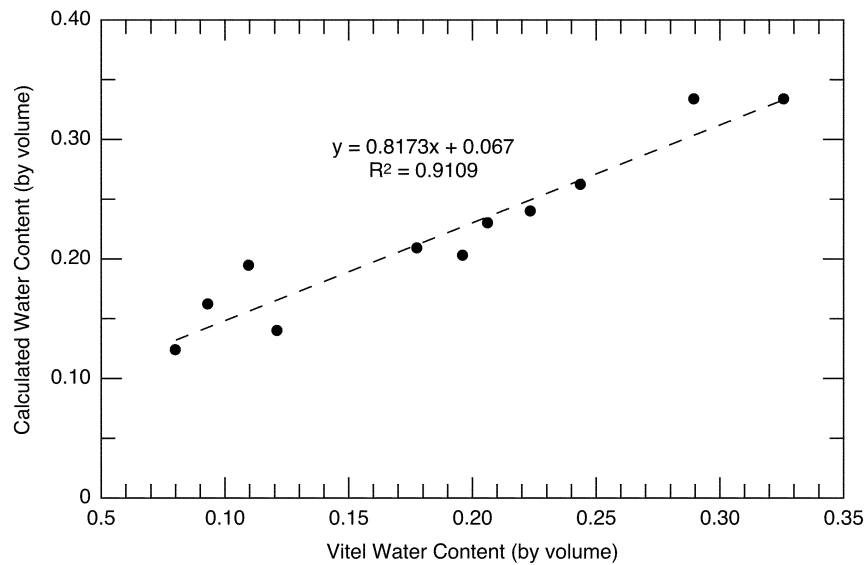
a. A-2-4 soil.
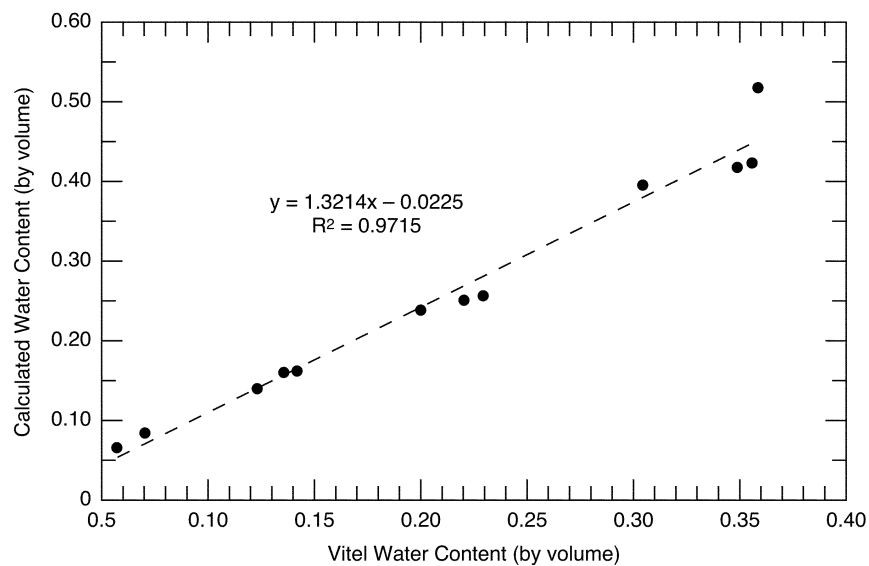
b. A-4 soil.

Figure 33. Calibration results of the Vitel gage for the test soils.
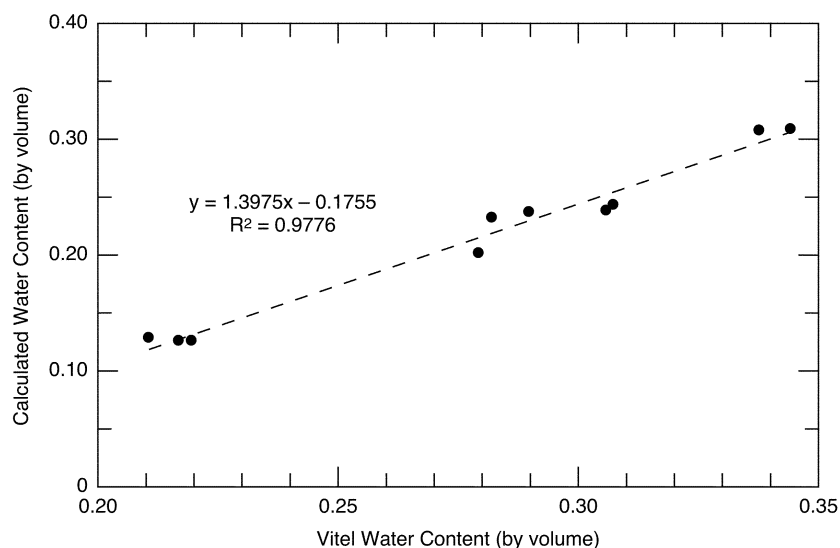
c. A-6 soil.
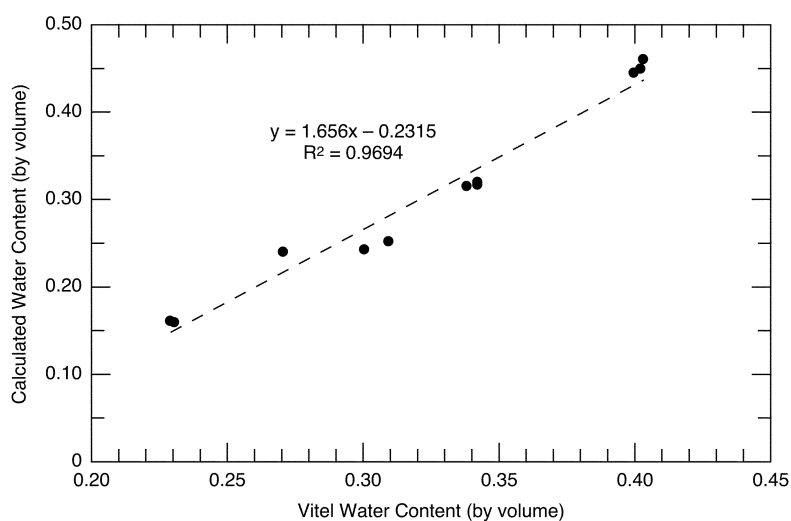
d. A-7-6 soil.

Figure 33 (cont.). Calibration results of the Vitel gage for the test soils.

There was some concern about using metal containers to do these tests. The volume of the metal container was considered to be low, and the metal walls could have affected the probe measurements. To check this, the metal container was immersed with a material whose dielectric constant is known, and measurements were taken with the Vitel gage. The medium used was water, which has a

dielectric constant of 80. The average value from three tests was 83, close to the dielectric constant of water. Therefore, any effect of the metal container was thought to be insignificant.

The volumetric water content of the sample was calculated by dividing the volume of water added in the sample by the volume of the sample. The volume of the sample is the volume of the container. This value was then compared to the value obtained from the results of the Vitel readings.

The following linear equations are used to determine the volumetric water content:

$$\text{A-2-4 } Vol = 0.8173 \times (Vitel) + 0.067 \qquad R^2 = 0.91 \qquad (4)$$

$$\text{A-4 } Vol = 1.3214 \times (Vitel) + 0.0225 \qquad R^2 = 0.97 \qquad (5)$$

$$\text{A-6 } Vol = 1.3975 \times (Vitel) + 0.1755 \qquad R^2 = 0.98 \qquad (6)$$

$$\text{A-7-6 } Vol = 1.6560 \times (Vitel) + 0.2315 \qquad R^2 = 0.97 \qquad (7)$$

where *Vol* is the corrected volumetric moisture content and *Vitel* is the measured volumetric moisture content (Vitel gages).

Dynatest stress cells

Dynatest soil pressure cells are double-diaphragm soil pressure gages. The stress gage uses a 350-Ω strain gage mounted on the titanium face of a fluid-filled cell (Fig. 34). Since the entire gage is machined from titanium, it is very stiff and has little or no hysteresis. The cells are manufactured for specific stress ranges: 10–200 kPa (Type A) or 100–800 kPa (Type B). Generally, we used the
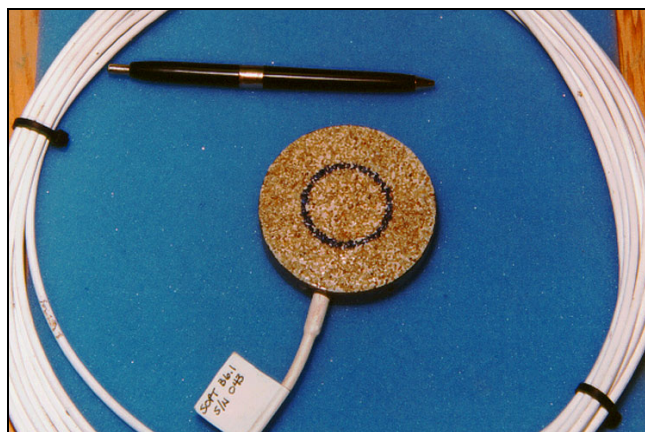

Figure 34. Dynatest soil pressure cell.

Table 13. Specifications for the Dynatest stress pressure cells.	
Construction material	Titanium
Sensor type	Hydraulic with pressure gage
Model	SOPT– 298/SOPT–XXX
Diameter	68 mm
Ranges	0–28, 28–113 psi
Excitation voltage	12 V
Resolution	Infinite

Type A gage to measure horizontal stresses and the Type B to measure vertical stresses. Some pertinent specifications of the gages as reported by Dynatest are shown in Table 13.

Prior to selection of this gage, a study was conducted to compare the responses of several types of gages available on the market in the U.S. and in Denmark. The study focused on sensitivity, linearity, hysteresis, conformance, and temperature drift. The evaluation was conducted in fluid (air), sand, and clay environments. Details of these tests can be found in Zhang et al. (1995) and Zhang and Selig (1995). A similar study was conducted by DRI (Askegaard 1995). The sensitivity of the Danish stress cell is approximately 2.2 mV/100 kPa, which is fairly low. However, the hysteresis between loading and unloading is minimal. This allows us to use one equation for calculating the pressure during loading and unloading. The output was linear with the applied pressure. Finally, the study found that the calibration curve developed for the fluid environment can also be used for either the compacted sand or clay (Fig. 35). Based on the
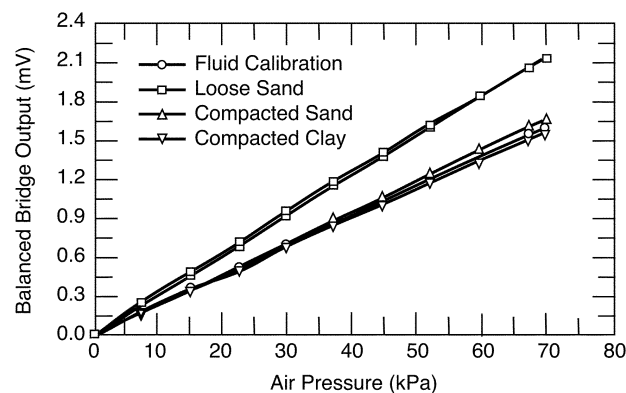

Figure 35. Typical calibration curves for Dynatest soil pressure cells. (After Zhang et al. 1995.)

study, we decided to use calibrations provided by the manufacturer for determining the stresses in all the test sections. These cells were found to be sensitive to temperature. We therefore decided to use these gages for measuring dynamic stresses only, where the gages will be nulled prior to measurement.

Since the stress cells will also be used to measure the horizontal stresses in the longitudinal and transverse directions, another study was conducted in the laboratory (Zhang and Selig 1995). It was concluded that the response of the soil pressure cells when measuring horizontal stresses may be influenced by the degree of compaction and the stress state. The data also suggest that the pressure cell, in most cases, overregisters the applied horizontal pressure. However, the authors also cautioned that this may have been caused by problems with the test equipment itself (Zhang and Selig 1995). Therefore, the same calibration curves used in the vertical direction are being used for the horizontal stress calculations.

Because of the limited number of pressure gages available, in most cases the gages are placed in a longitudinal (X), transverse (Y), and vertical (Z) configuration (Fig. 36) at either one or two depths below grade (46 and 76 cm) in the test sections. In special cases, pressure cells are placed 107 cm below grade in the Z direction and 19 cm below grade (within the base course) for X, Y, and Z. The Z-direction stress cell has the sensing element facing in the vertical direction. The X-direction stress cell has its sensing element facing in the direction of wheel travel. The Y-direction stress cell has its sensing element facing transverse to the direction of wheel travel.
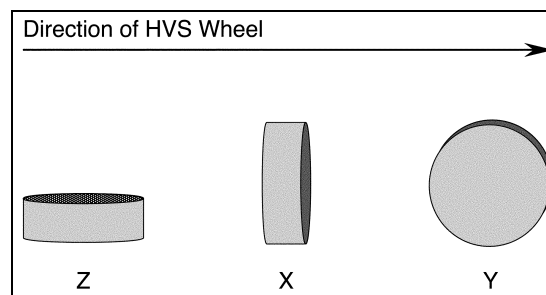
Figure 36. Soil pressure cell placement in the vertical (Z), longitudinal (X), and transverse (Y) directions.

The vertical stress cells are placed on the compacted subgrade and covered with lightly tamped soil. For the horizontal cells, we are following the procedure developed at the RTM in Denmark. First, a "dummy" cell, which is slightly smaller than the actual cell, is embedded halfway into the soil layer. The dummy is then removed and the actual sensor installed. The stabilizing rods provided by

the manufacturer are not used in soils compacted at or near optimum. However, they are used in subgrade soils where the placement moisture content is wetter than optimum. Stress data were collected at a sample rate of 400 Hz. Typical dynamic stress measurements at the top of the subgrade are shown in Figure 37.
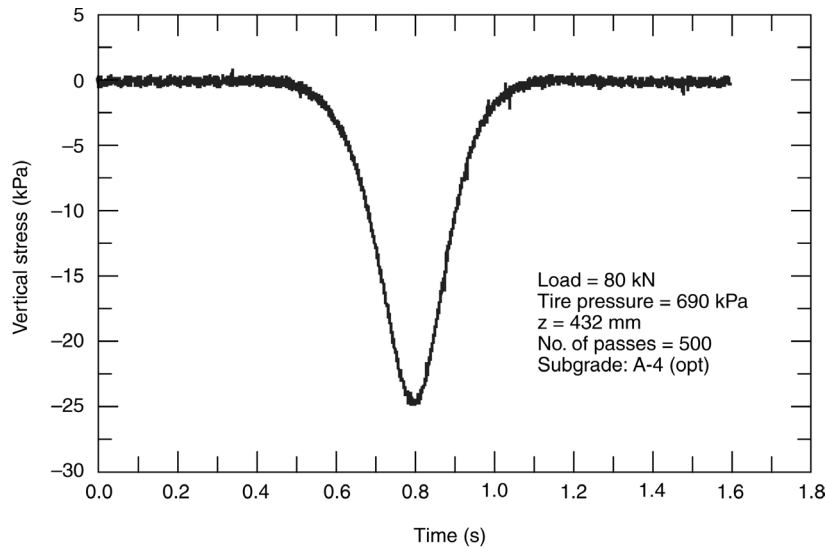
a. Vertical.
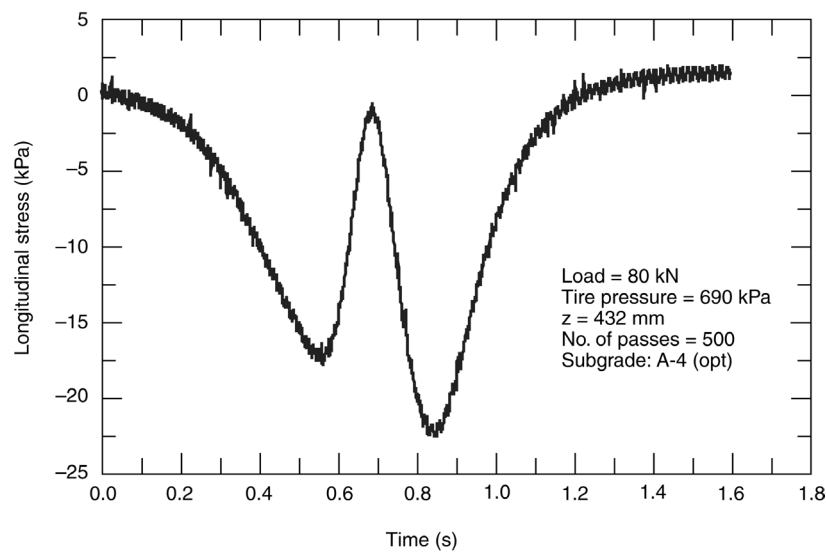
b. Longitudinal.

Figure 37. Typical stress measurements in the subgrade.
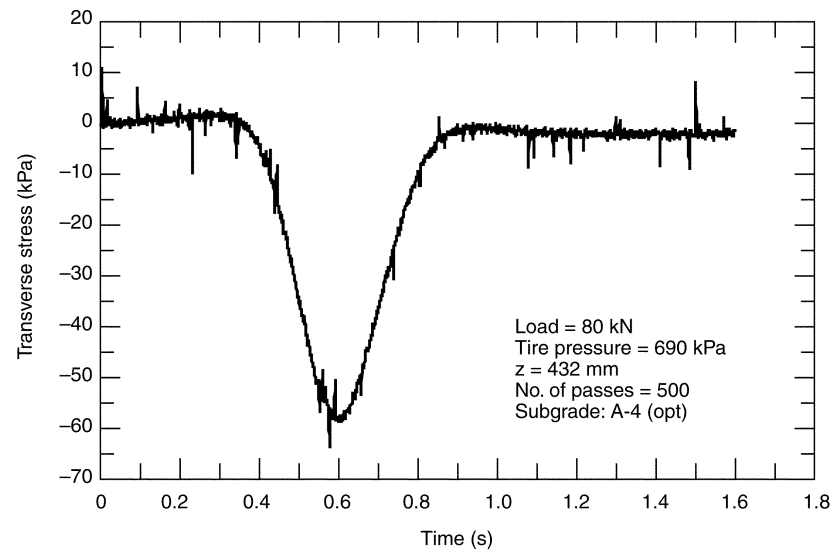
c. Transverse.

Figure 37 (cont.). Typical stress measurements in the subgrade.

Geokon stress cells

Several Geokon earth pressure cells (Fig. 38) were used to measure the dynamic pressures in the base layer. Dynatest pressure cells were not used in the base course layer because this layer was constructed with crushed rock with a maximum size of 50 mm, and the ratio of the diameter of the Dynatest pressure cell to the maximum rock size was close to one. This was sufficient cause of concern for non-homogeneous effects on the stress measurements.
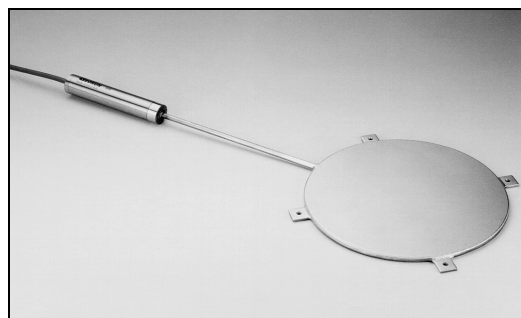
Figure 38. Geokon soil pressure cell.

Geokon pressure cells consist of two circular stainless steel plates welded together around their periphery and spaced apart by a narrow cavity filled with either an antifreeze solution or mercury. A length of high-pressure stainless steel

tubing connects the cavity to a pressure transducer. The internal fluid is degassed to a maximum dissolved gas content of 2.0 ppm. This ensures that the volumetric displacement of the cells is kept to a minimum and that the response characteristics are linear and sensitive. These pressure cells are usually used for measuring long-term in-situ static pressures and commonly use a vibrating wire pressure transducer. Since we wanted to measure dynamic pressures in the base layer, the pressure transducers for our cells were converted to a strain-gage-based system for faster response time. The external pressures on the cell are balanced by an equal pressure induced in the internal fluid. The internal pressure is converted by the pressure transducer into an electrical signal, which is transmitted by a four-conductor shielded cable (direct burial type) to the readout location. A typical measurement of the stress in the vertical direction in the base is shown in Figure 39.
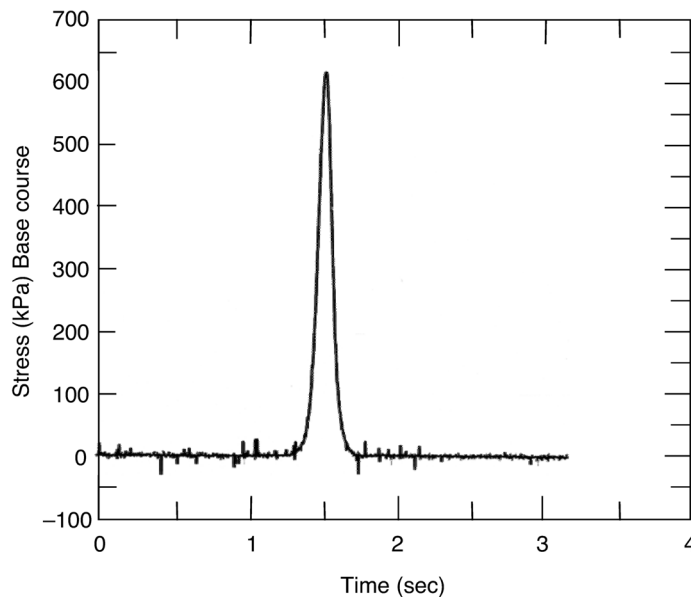
Figure 39. Typical stress measurements in the base course layer (Z = 150 mm, tire pressure = 690 kPa).

Emu soil strain measurement system

The emu system that is used for measuring triaxial dynamic and permanent deformation in the base and subgrade in the FERF is shown in Figure 40. It consists of one sending coil and three receiving coils (longitudinal, transverse, and vertical), the emu signal conditioner, and a computer data acquisition system. Details of the system can be found in the users manual by Dawson (1994).
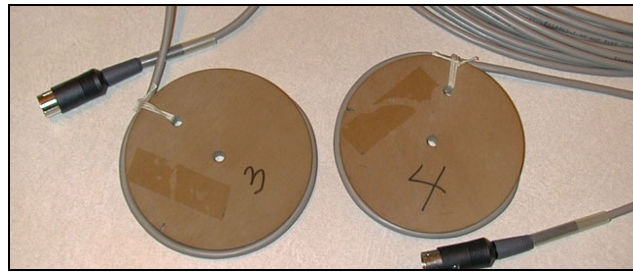
Figure 40. εmu soil strain measurement coils.

The system is based on the principle that when an alternating current is passed through a coil of wire, an alternating magnetic field is generated. Another coil placed within this field will have an alternating current induced in it. The magnitude of the induced current is proportional to the magnetic flux density, which in turn is nonlinearly related to the distance between the two coils. Thus, a pair of sending and receiving coils provides a non-contacting displacement, or strain, measuring device.

The coil sensors were made at CRREL by winding 18-gage copper wire for 80 turns around the edge of a robust 100-mm-diameter epoxy disc (which is unaffected by moisture). After manufacture, the coils were potted and sealed to protect the junction with a coaxial cable, which was 25 m long. The resistance and inductance of each coil and cable were measured, and those coils that substantially departed from the norm were discarded.

The εmu signal conditioner contains the power supply, a high-frequency a.c. oscillator (in the 14-kHz range), and the electronics for demodulating the output signal from the coil pairs. Three demodulating channels each provide a static output that relates to the coil spacing (and hence gives a measure of permanent deformation) and a dynamic output that gives an amplified trace of the transient deformation (and hence dynamic strain) under traffic loading. Both the static and the dynamic amplifiers provide separate, continuous, d.c. voltages, which can be logged by an analog-to-digital (a/d) data acquisition system in a computer. A separate triggering signal is needed to actuate the data acquisition system as the moving wheel approaches.

One signal conditioner can demodulate the response from up to three receiving coils. We are using the three demodulation channels to simultaneously measure the displacements in the longitudinal, transverse, and vertical directions of traffic at several depths beneath the surface. To accomplish this with one signal conditioner, the cables for each depth are attached to the signal conditioner through a multiplexing relay.

The data acquisition system consists of a 486-based PC with a Keithley/MetraByte data acquisition card (DAS-1800HR-DA) and a pair of Omega PIO-24 relay multiplexers. The cables from the coils are plugged into a panel connected to the relay multiplexers. The output from the multiplexer is connected to the coil excitation output and the three receive inputs of the εmu system. The "static" outputs from the εmu signal conditioner are connected to the Keithley a/d board. For the "dynamic" signal outputs, a noise-reducing filter system is placed in-line between the εmu system and the Keithley a/d panel.

The Danish Road Institute conducted preliminary studies on different types of stress and strain instrumentation to be used in the study (MacDonald and Baltzer 1997). They compared their standard LVDT-based system versus the εmu coil-based system to measure strains in the RTM test sections. They found that the displacement response collected by the εmu system suffered from both electrically induced and magnetically induced noise.

### Effect of electrical noise

The high-frequency electrical noise originated from a motor on the load cart, from the fluorescent lights, and from arcing on the high-voltage mains that provided electricity to the load cart. The static response from the coils was not affected by this problem because the load cart was not running when the permanent deformation was being measured. Also, noise is not a problem for static measurements because the εmu signal conditioner uses a lower signal amplification gain. The dynamic response, however, was almost totally masked by the electrical noise. It was evident that a low-pass filter system was needed to remove the electrical noise from the dynamic signal.

The apparent strain that is caused by metal moving through the magnetic field is, in effect, magnetic noise. As with the electrical noise, it only affected the dynamic strain signal. However, because it is caused by the moving wheels, its frequency is very similar to the signal that we seek to measure. Thus, low-pass signal filtration would not be appropriate for removing the magnetic noise.

In the FERF the electrical noise comes mostly from the lights and the air handlers, at a frequency of 60 Hz. The HVS does not have the same electrical arcing problems associated with the RTM. We felt that with the proper choice of cables and in-line analog filtering, we could reduce the effect of the noise on the measurement to an acceptable level.

The dynamic signal from the εmu signal conditioner was filtered through an analog, low-pass, programmable elliptic filter with a cutoff frequency set at 40 Hz. We used an elliptic eight-pole filter to give the greatest reduction in fre-

quency response. One problem with this type of filter is that it has a frequency-dependent delay. Therefore, the noise reduction is a function of two variables: the corner frequency (f_r) and the delay. The functions for these variables are shown in Figure 41. It can be seen in Figure 41b that the time delay is essentially constant up to $0.3\,f_r$. Choosing 40 Hz for the cutoff frequency gave a constant delay
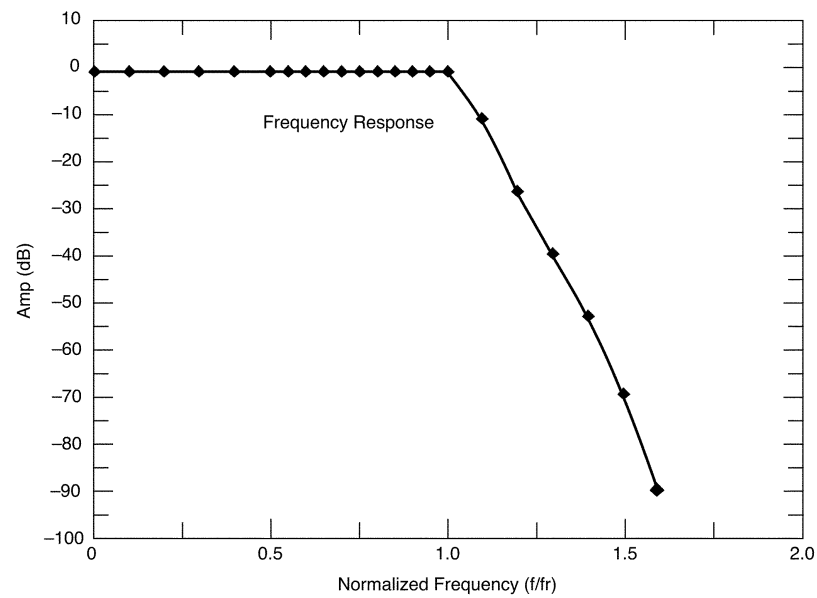
a. Frequency response of analog filter.
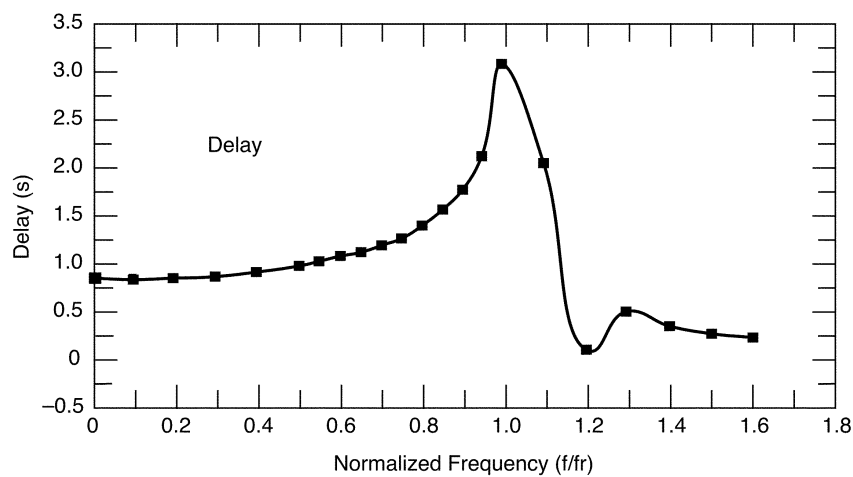
b. Delay of input signal as a function of frequency.

Figure 41. Variables affecting noise reduction in the Ɛmu signal conditioner.

from 0 to 12 Hz and a noise reduction of 70 dB (less than 1/1000 of the signal) at 60 Hz. Given the HVS loading speed of roughly 15 km/hr, our dominant measurement frequency was around 4 Hz, which is well within the 12-Hz constant delay. Thus, we concluded that the filter system would have no adverse effect on the accuracy of the dynamic signals from the εmu system.

Typical results for dynamic vertical, longitudinal, and transverse strains, filtered and unfiltered, are shown in Figure 42. The residual effect of the electrical
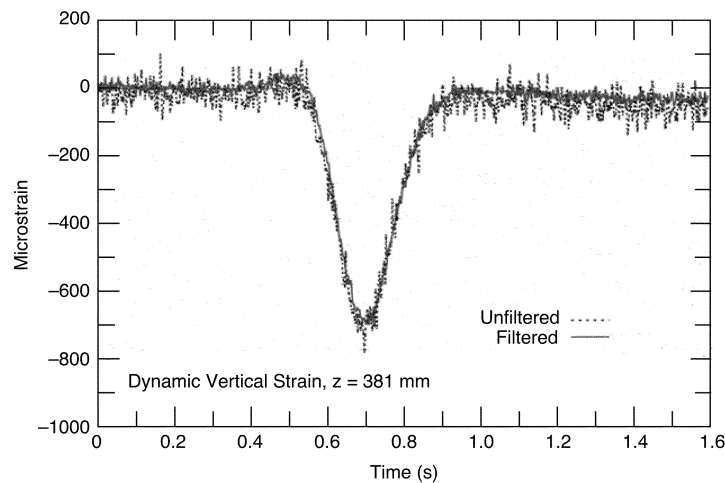
a. Dynamic vertical strain at 381 mm from the surface of the AC layer.
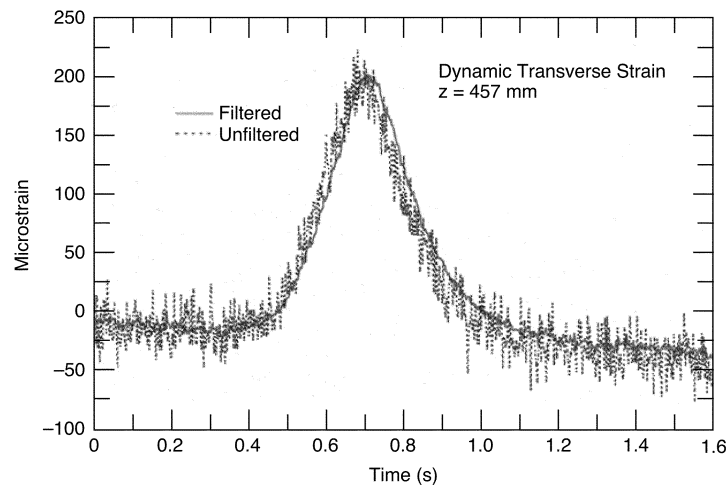
b. Dynamic transverse strain at 457 mm from the surface of the AC layer.

Figure 42. Effect of analog filtering.
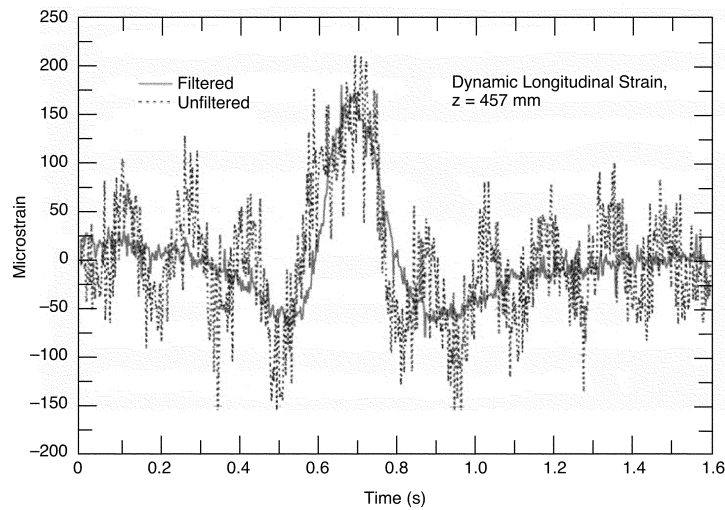
c. Dynamic longitudinal strain at 457 mm from the surface of the AC layer.
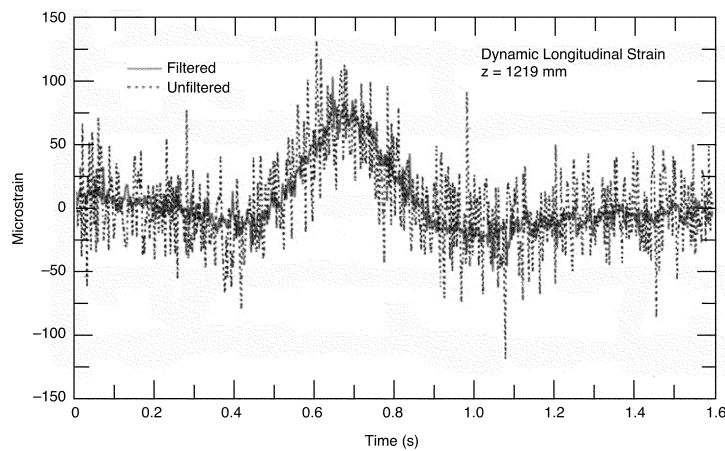
d. Longitudinal strain at 1219 mm from the surface of the AC layer.

Figure 42 (cont.). Effect of analog filtering.

noise on strains greater than 700 microstrains was minimal. With the effective reduction of electrical noise, we were able to adopt a strategy similar to that used by DRI to minimize the effect of the moving metal.

Effect of the moving wheel carriage

To study the effect of the moving, loaded HVS wheel, a large number of dynamic measurements were taken at several depths. Then an equal number of

measurements were taken for each coil pair with the wheel traversing the test section at approximately 50 mm above the pavement surface. The corrected dynamic signal is the difference between the load and no-load signals.

To average the results of several replicate tests, we used a Microsoft Excel spreadsheet. We decided not to automate the process since it requires visual inspection of the data. All test results were visually checked prior to use.

The effect of the moving wheel carriage on the dynamic vertical and longitudinal strain is shown in Figure 43. The results shown are typical for all depths of measurement. In every case the "no-load" (i.e. carriage traverse without loading) response is insignificant compared to the response measured under the loaded wheel. This is especially the case with respect to peak response.

The effect of the moving carriage on the transverse strain is shown in Figure 44. At high strain levels (e.g., near the surface) the effect of the moving metal was minimal (Fig. 44a). However, at low strain levels (at larger depths) the effect of the no-load signal was more significant (Fig. 44b).
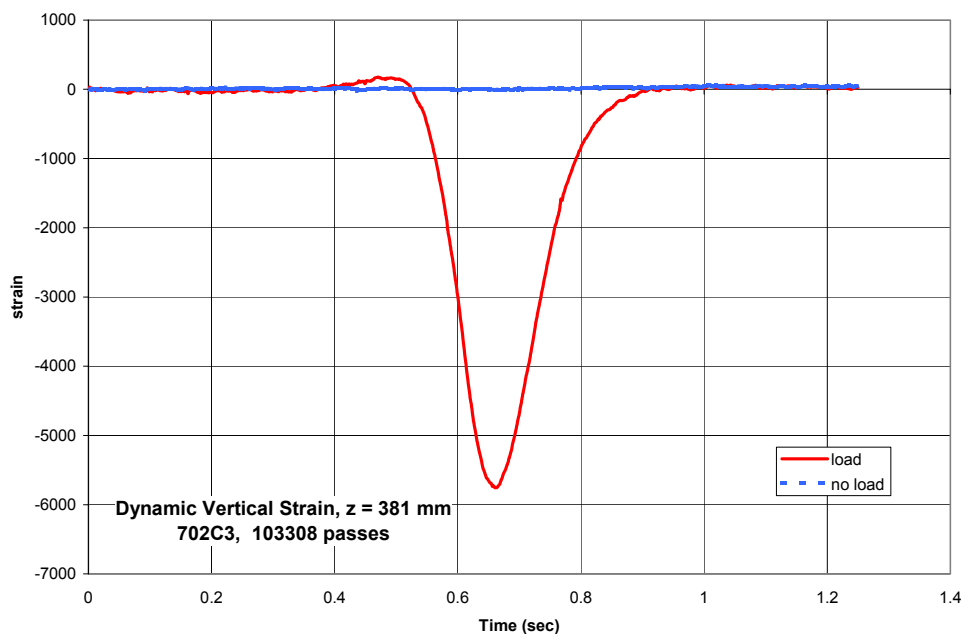
a. Vertical strain at 381 mm from the surface of the AC layer.

Figure 43. Effect of the moving carriage on vertical and longitudinal strain.
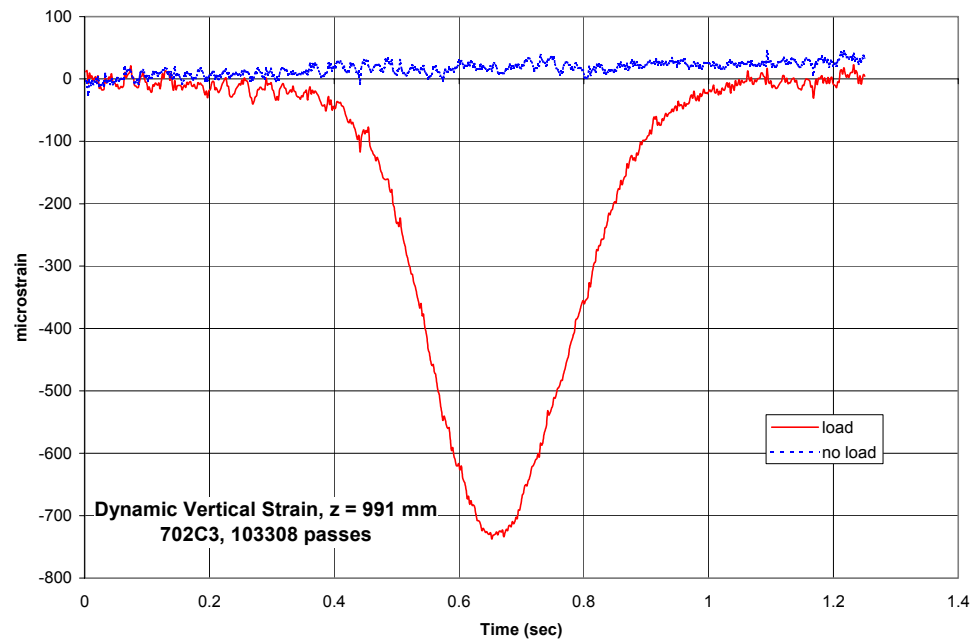
b. Vertical strain at 991 mm from the surface of the AC layer.

c. Longitudinal strain at 381 mm from the surface of the AC layer.

Figure 43 (cont.). Effect of the moving carriage on vertical and longitudinal strain.

d. Longitudinal strain at 914 mm from the surface of the AC layer.

Figure 43 (cont.). Effect of the moving carriage on vertical and longitudinal strain.

a. 305 mm from the surface of the AC layer.

Figure 44. Effect of moving carriage on transverse strain.
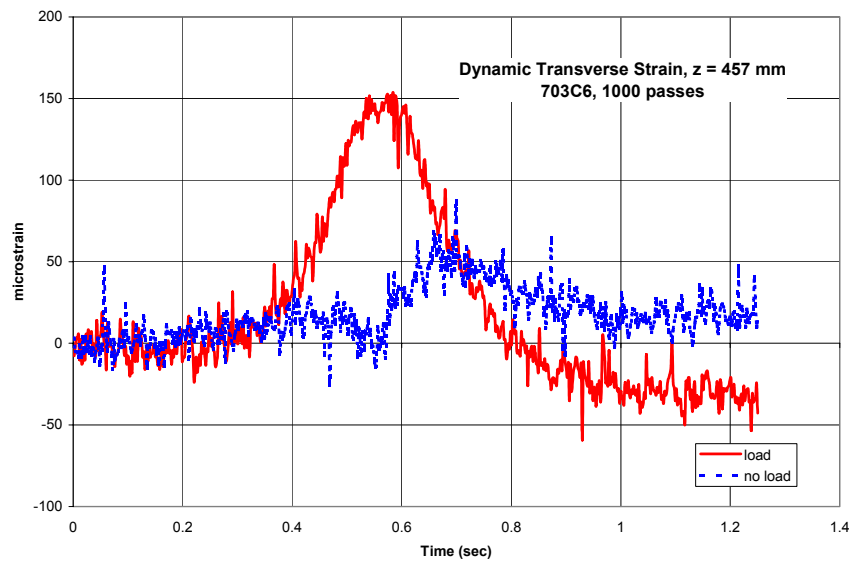
b. 457 mm from the surface of the AC layer.

Figure 44 (cont.). Effect of moving carriage on transverse strain.

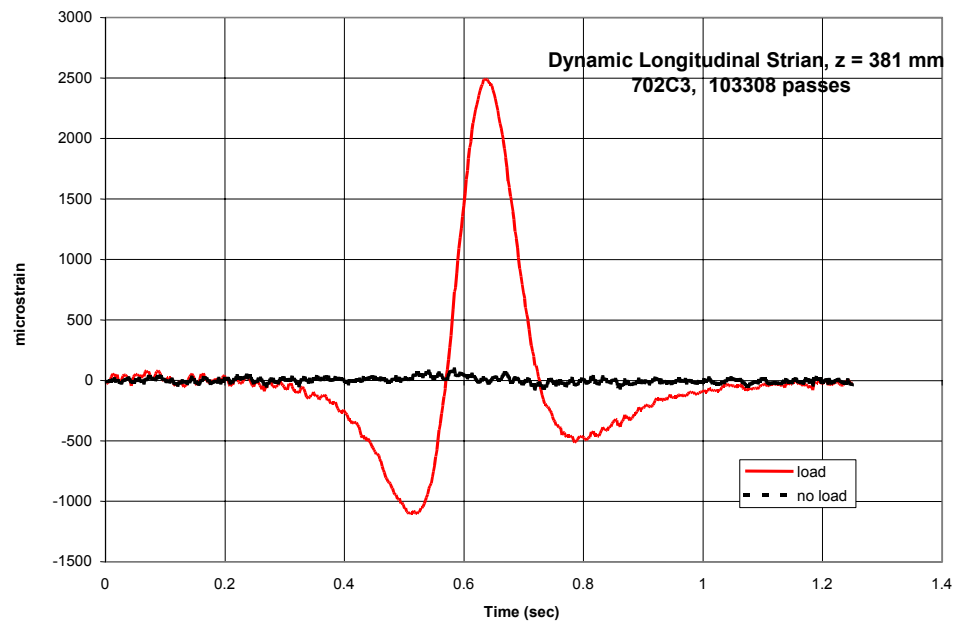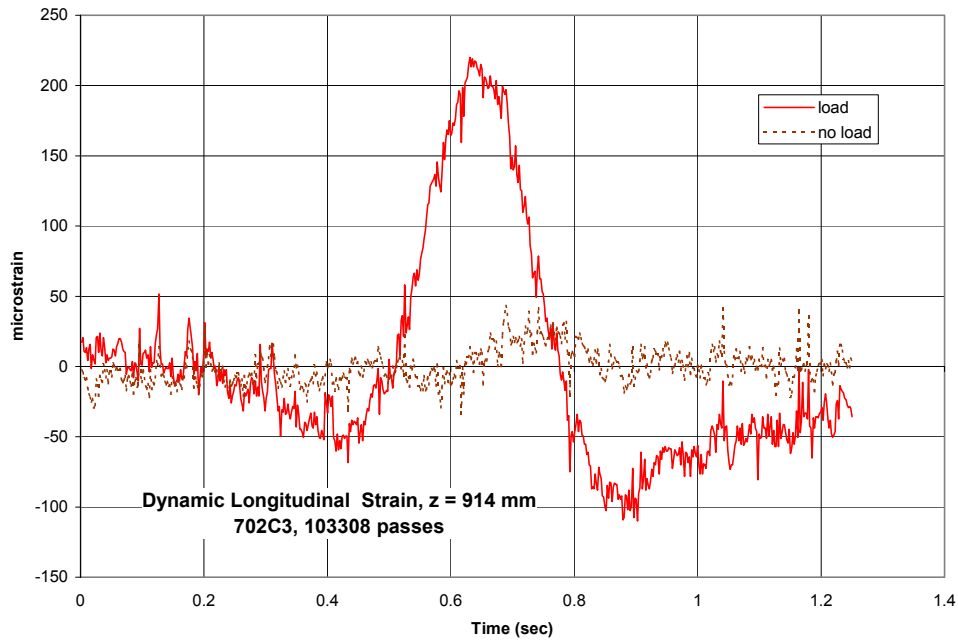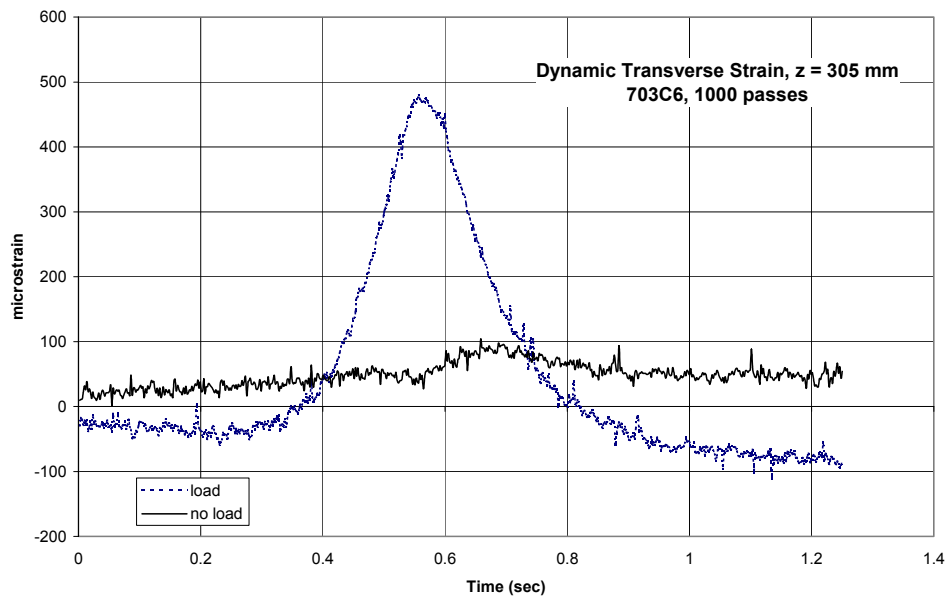Even though the effect of the moving metal was apparently quite small, it was decided to correct the time histories for all strains by subtracting the no-load signal from the full-wheel-load signal. From the results of the initial study we decided to take five dynamic time histories for each triaxial coil pair at each depth and average them using the spreadsheet. Then five measurements were taken for each coil pair with the wheel traversing the test section without loading the pavement. The corrected dynamic time history is the difference between the load and no-load signals.

After the corrections for the magnetic noise and the moving metal, we found that the shape of the dynamic time histories in all directions were the same as those produced by the LVDT-based sensors in the Danish Road Institute RTM.

Effect of coil rotation and misalignment

While removing the coil sensors after an accelerated load test, we discovered that it is possible for the coils to rotate and move out of alignment as the soil undergoes permanent deformation. Such movement or rotation can produce false deformation readings, incorrectly indicating the true center-to-center spacing between the coils. A study was conducted in the lab to investigate the effect of rotation and translation between the coils on the apparent strain, in both the coaxial and coplanar configurations.

Using the calibration jig in the coaxial plane, two scenarios were tested. Scenario one involved rotating one of the coil pairs in the horizontal (X-Y) plane. The second scenario was to allow one of the coils to move laterally in the horizontal plane. The tests were conducted to a maximum tilt of 8° (scenario one) and a lateral displacement of approximately 25 mm (scenario two). These ranges were based on observations of actual movements.

The initial distance between the coils was 152 mm. The results are shown in Figure 45. The largest apparent strain indication occurred around a 3° tilt and then changed from negative to positive with increasing tilt. The error from our study was less than 1%, or about a 1-mm error in a 150-mm gage length. Patterson (1972) reported from a similar study that a 10° rotation produced an error of 1.2% indicated strain. Review of his data further found that a rotation of up to 20° produced an error of 5% indicated strain. With respect to lateral displacement in the coaxial alignment, the strain increased by approximately 2.5% when the lateral displacement was 25 mm (1/4 coil diameter).

Similar tests were done with coplanar coils, with the receiving coil tilted, the transmitter coil tilted, and with the receiving coil parallel but off axis. Figure 46 shows that the effect on the strain was minimal. The combined effect of tilt (8°) and lateral movement at 12 mm indicated a maximum variation of 2% on the calculated strain.

Coil rotation and misalignment have been observed to occur simultaneously during large plastic strains due to traffic loading. Based on the measured effects of rotation and misalignment we concluded that the practical minimum sensitivity of the coil system is about 1 mm of permanent deformation in a 150-mm gage length.

Installation of coil sensors

In the FERF, sets of 100-mm-diameter coil sensors are installed at six locations in the base course and subgrade. They measure the displacements in the vertical direction (designated as the Z direction) and in two perpendicular horizontal directions (X and Y directions), as shown in Figure 47.

The coils are installed at nine depths in columnar stacks, starting at 150 mm below the pavement surface and extending to 1.35 m at a nominal center-to-center spacing of 150 mm. A loose coil can be temporarily placed on the asphalt surface to measure the permanent deformation in the upper layer of asphalt and base.

a. Tilt.
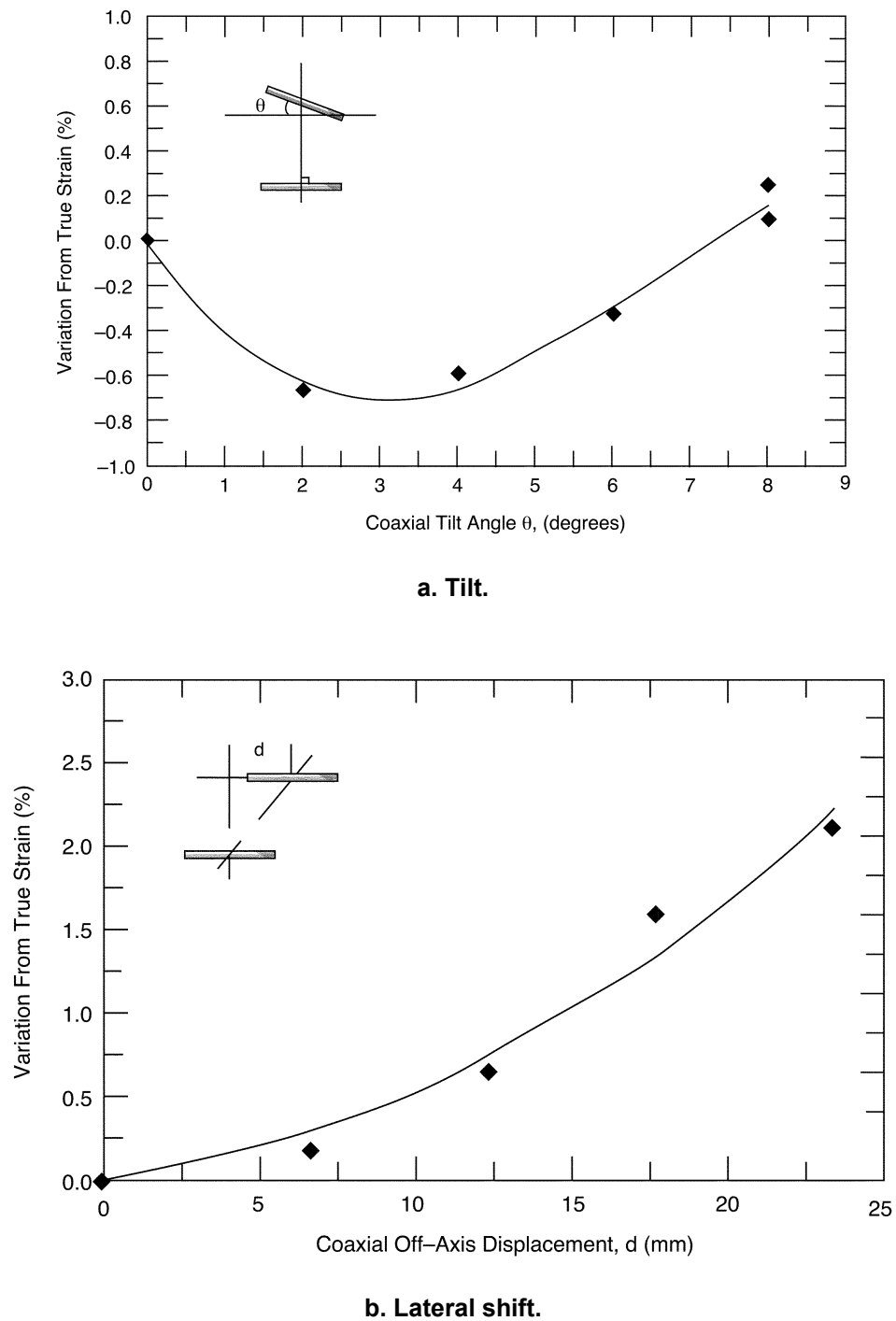
b. Lateral shift.

Figure 45. Effect of movement of the coaxial coils on calculated strains.
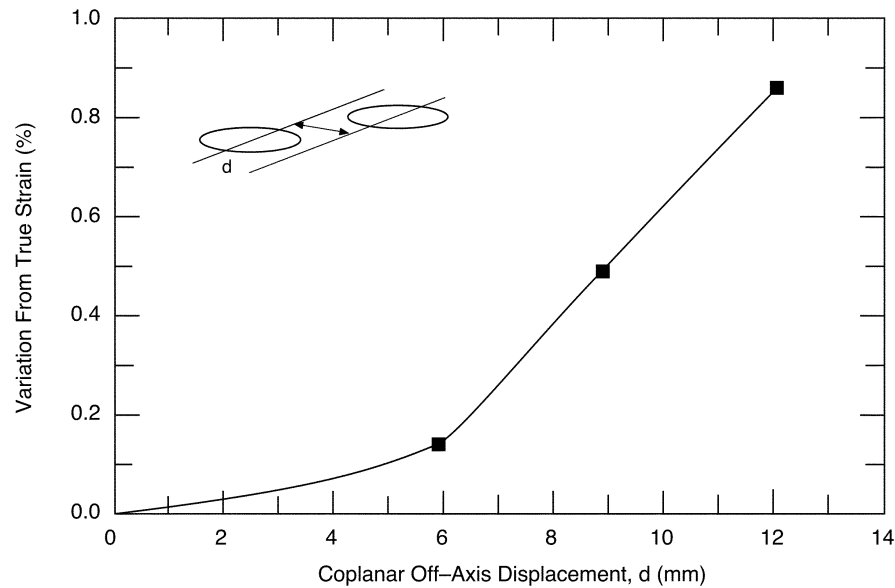
Figure 46. Effect of lateral shift of coplanar coils on calculated strains.

Figure 47. εmu coil placement in a test section.

The Z-direction coils are coaxial, while the X- and Y-direction coils are co-planar. The X direction is parallel to the wheel travel, and the Y direction is perpendicular to it.

During installation, the surface where the coils were to be placed is raked smooth and level before coil placement. To assure that the coil is aligned coaxi-ally with the coil immediately below, the next lower coil is excited and the static

response from the upper coil is measured. The coils are aligned when a maximum output from the coil pair is achieved. The coil is pressed down on the surface, checked with a carpenter's level, and shimmed with soil, if necessary, to assure that it is level.

The thickness of the underlying compacted lift of soil is then measured. A thickness of approximately 150 mm is desired. If the lift is too thick, a small amount of trimming is done in the area where the coil is placed. If the lift is too thin, a small amount of shimming with soil is done. After the coil is properly aligned and leveled, it is covered with about 5 cm of soil, which is lightly tamped. The coaxial cable leading to the coil is routed in a small trench, with a strain-relieving loop in the cable. The alignment dowels, visible in Figure 47, are then removed, and a 150-mm lift of compacted subgrade soil or base course is constructed using normal construction procedures.

Static and dynamic coil sensor calibration

To relate the output voltage to the coil spacing in engineering units (millimeters), the pairs of coil sensors must be calibrated. The coils were calibrated statically (simulating permanent deformation) and dynamically (simulating elastic strain) in one of two positions, either coaxial or coplanar. A calibration jig (visible in the foreground in Figure 48) is made of plastic, with the exception of the micrometer head.

For coaxial calibration the transmitting coil was placed on the left end, away from the micrometer head, and the receiving coil was placed on the moveable frame, as shown in Figure 48. In the coplanar position the coils were placed as shown in Figure 49. For the coaxial position the coils were initially spaced 140 mm apart, measured from the center of thickness of each coil. In the coplanar position the coils were also initially spaced 140 mm apart, measured from the centers of the coils.

The transmitting coil was excited by the εmu signal conditioner. The receiving coil was connected to the appropriate εmu detector unit. The amplifier time constant was set to fast, and the static output was monitored. Voltage measurements were made with a Hewlett Packard 3478 5-1/2-digit multimeter. Voltage measurements were taken after coil displacements of 0, 6.35, 12.1, 19.0, and 25.4 mm by adjusting the micrometer head. Therefore, the coil spacing varied from about 140 to 165 mm. The coils were placed in the ground at 152-mm spacing.

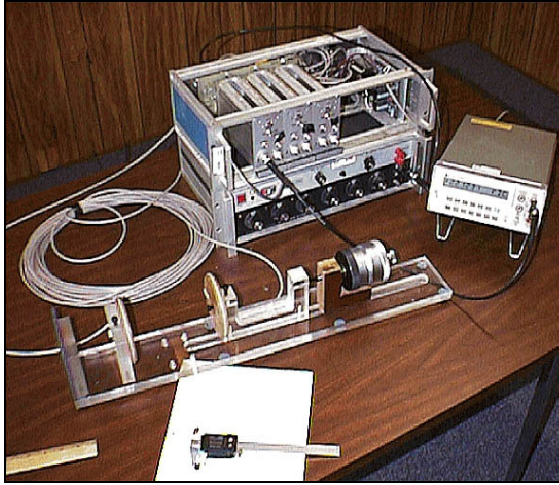The following power equation gave a good fit to the calibration data:

$$V = a\ D^n \tag{4}$$

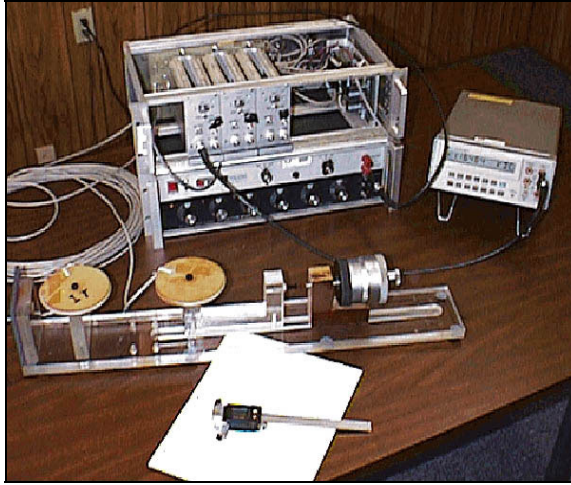**Figure 48. Calibration system of coaxial coil gages.**

Figure 49. Calibration of coplanar coil gages.

where D =   static distance between the transmitting and receiving coils
           V =   demodulated (d.c.) "static" voltage from the coils
  a and n =   regression constants for a pair of coils.

Typical static calibration curves for the coaxial and coplanar gages are shown in Figure 50. Provided that the coils remain coaxial or coplanar, these calibrations will give the center-to-center spacing of the coils when there is no traffic load. By taking measurements after various numbers of load repetitions, the change from the initial spacing between the coils can be determined, and hence the permanent deformation and the permanent strain can be computed.

We found that the static spacing between two coils can be measured to the nearest 0.025 mm or better for a coil spacing of 150 mm. Irwin et al. (1985) reported the same finding when using the Bison system. Thus, it is hypothetically possible to detect a permanent deformation as small as 0.025 mm. However, some alignment limitations discussed below will result in a larger minimum sensitivity.

The calibration for the transient deformations and strains under traffic load can be obtained directly from the static calibration by taking the first derivative of eq 4:

$$\Delta V = c\, D^{n-1}\, \Delta D \tag{5}$$

where ΔV =   dynamic voltage at any instant in time during the load pulse

ΔD = change from the static distance between the coils (dynamic deformation)

c = constant that is a function of the gain setting on the amplifier.

Detailed procedures for the static and dynamic calibration of the coil sensors can be found in the users manual by Dawson (1994).
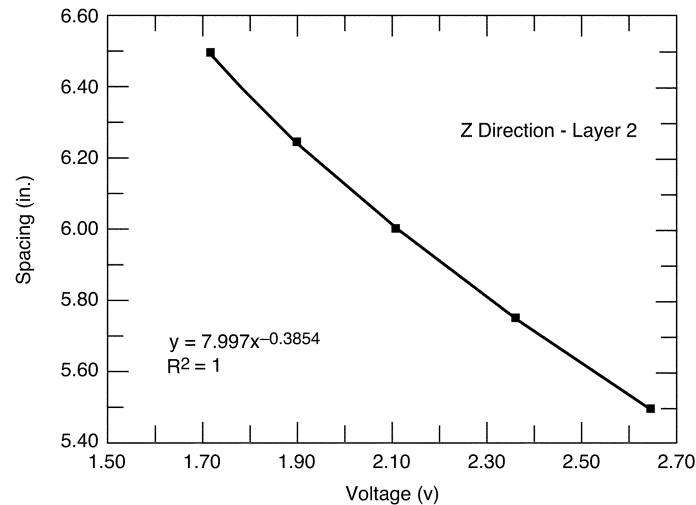
a. Coaxial (vertical direction).
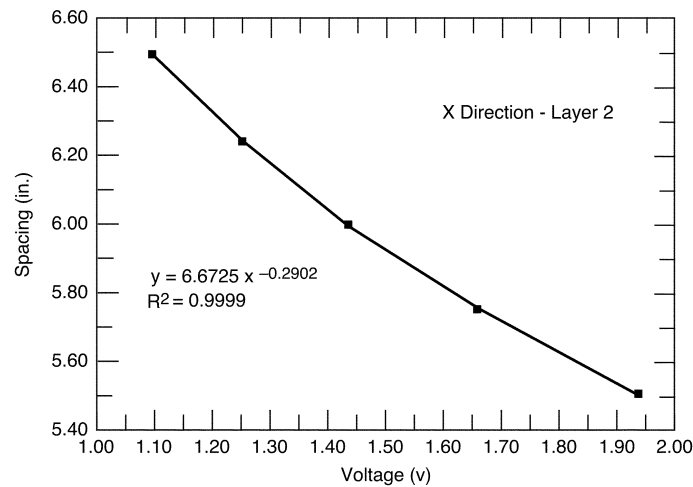
b. Coplanar (longitudinal direction).

Figure 50. Typical calibration curves for the εmu gages.

Surface deformation measurement system

Surface deformations are being measured using the Council Scientific Industrial Research (CSIR) profilometer. It is a beam approximately 3 m long with a stepper motor/cable system that moves a small carriage on the beam (Fig. 51). The beam rests on three feet and is about 45 cm above the ground. The feet are placed on the same specially marked areas on the ground when measurements were taken at different pass levels. In addition, level surveys were conducted on the marked areas to determine any vertical movement. Mounted on the carriage is a small infrared laser range finder. The computer program controls the speed of the carriage and collects 256 range data points over the length of the run (approximately one point every 9 mm) as the carriage traverses the test section. Twenty-four cross section measurements, at 0.3-m intervals, starting at one end of the test section are taken and stored in a file for transfer to the main data system. Figure 52 shows the development of the rut with number of load repetitions.

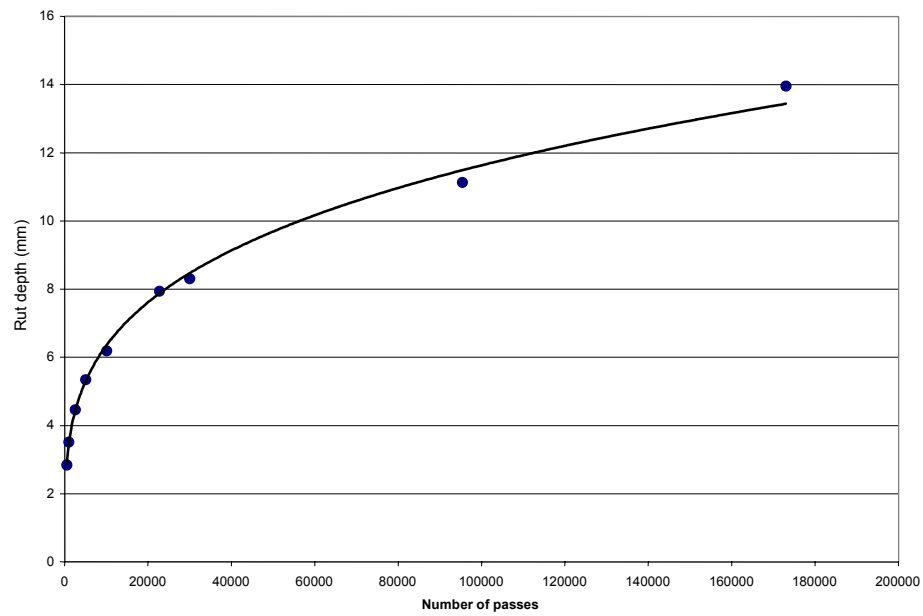**Figure 51. CSIR surface deformation measurement system.**

Figure 52. Example of rut development as a function of number of passes.

9   DATA ACQUISITION SYSTEM

The data acquisition system for the overall project consists of four subsystems. One system collects data (time, load, speed, tire pressure, tire temperature, number of passes) from the HVS. The second collects the surface and subsurface temperature and moisture data. The third is the dynamic stress, permanent strain, and dynamic strain data acquisition system. The laser-measured rut depths are collected on a fourth data acquisition system.

The FERF has several Campbell Scientific dataloggers in place. For this project two CR10, one CR7, and one CR21X dataloggers are used. The CR10 is equipped with a minimum of one 32-channel differential multiplexer. The CR7 and the 21X have 16 differential input channels. These dataloggers are ideal for reading voltages in the range of ±2.5 mV to ±2.5 V full scale with the CR10 and ±1.5 mV to ±5.0 V with the CR7 and 21X. These dataloggers are ideal for "slow" measurements in that their fastest data throughput is 64 Hz per channel. Sensors that fall within these ranges are thermocouples, thermistors, sensors that have half or full bridges, and any sensor that generates a voltage within this range. Most sensors can also be signal conditioned so that their output falls within the required range. These dataloggers are ideal for the temperature and moisture measurements.

The Campbell systems that are now in place are connected together and to a computer with an Ethernet-like coax connection. Downloading of data can be scheduled or at the operator's command for any and all of the systems on the net. Programs can be modified and real-time data can be displayed.

The computer that controls the operation of the HVS also collects operating data during the test. The data collected consists of the current pass number of the current test, the date and time, the average load for the pass, the average tire temperature for each tire, and the average tire pressure for each tire. These data are collected from pressure and temperature sensors within the tires and on the load carriage by a data system within the carriage and are transmitted along rails to the cabin and the control computer. The data are then transferred by network to the main data system.

Dynamic stress and strain data acquisition system

The computer data system consists of a 486-based PC with a Metra-Byte/Keithley data acquisition card (DAS-1800HR-DA) and a pair of Omega PIO-24 relay multiplexers. The cards are programmed using Quick Basic 4.5. The specifications for the data acquisition card are shown in Table 14. The

Table 14. A/d specifications for the DAS-1800HR-DA.	
Number of analog input channels	16 single ended or 8 differential
Resolution	16 bits
Speed	100 ksamples/s
Analog outputs:	2 DC level, 16 bits
Digital I/O	4/4
Input ranges:	
Bipolar	±10, ±5, ±2.5, ±1.25 V
Unipolar	0–10, 0–5, 0–2.5, 0–1.25 V
Absolute accuracy:	
Typical	±0.005% of reading ±1 LSB
Maximum gain>1	±0.01% of reading ±1.5 LSB
Relative accuracy:	
Typical	±0.001% of reading ±1 LSB
Maximum for 0–70°C	±0.001% of reading ±1.5 LSB

Dynatest stress cells plug into a rack of strain gage amplifiers with a fixed gain of 500, whose outputs are connected to the Keithley a/d panel. The coils for the εmu system plug into a panel connected to the relay multiplexers. The commons of the multiplexer are connected to the transmitter output and the three receiver inputs of the εmu system. The static outputs from the εmu are connected to the Keithley a/d panel. The dynamic outputs from the εmu are connected to a 40-Hz elliptical low-pass filter and to the Keithley a/d panel. Breaking a light beam outside the test window triggers the data acquisition system to begin collecting data. Data are collected for 1.5 s.

Data management

The raw data from the test sections and from the HVS are stored in several locations. One set is stored on the CRREL Oracle database. The second is stored on one-gigabyte Iomega Jaz disks and CDs.

10   DATA ANALYSIS AND MODEL DEVELOPMENT

The principal objective of this research is to develop pavement response models for permanent deformation that will allow pavement designers to predict rutting. Thus, model development is an essential part of the project. The model development will continue throughout the research program.

The currently used failure criterion for pavement rutting is the vertical strain on the subgrade surface. This will be a point of departure for model development for this research. However, it is planned to study the effectiveness of other stress- and strain-related parameters, such as those currently in use in flow theory and plastic theory. Since long-term pavement deformation is a plastic rather than an elastic phenomenon, it is expected that plasticity might offer a superior approach for predicting pavement rutting. An extensive effort will be made to postulate and test suitable constitutive models for predicting pavement rutting.

An important consideration is the implementability of the model(s) in future AASHTO design guides. The models must not be too complex, nor should they require complicated laboratory testing that is substantially beyond the capability of state highway agencies.

Several ongoing pavement field studies will be used to validate the models that will be developed. These include the LTPP project, the MNRoad project, and the TPPT project in Finland. The LTPP project has established 64 instrumented pavement sites where subsurface moisture and temperature will be recorded. Monthly data on profiles and FWD deflections are also being obtained. It is not certain that these test sections will be of use in the model verification since most, if not all, of the sections were built with a thick pavement cross section and there may not be much pavement rutting at these sites.

The MNRoad project is extensively instrumented. Some of the pavement sections are of a low-volume design on an A-6 subgrade, and they are expected to fail in three to four years. Other test sections are of a high-type design with five- and ten-year design lives. The low-volume road sections will have controlled traffic loading in a natural, uncontrolled environment. It is anticipated that the low-volume test sections at the MNRoad project will be especially useful for model verification, but the subgrade soil is essentially of a single classification.

The Finnish Pavement Structure and Subgrade Research Program (TPPT) may offer a considerable amount of additional data that could be used for model verification. The TPPT project was begun in 1993 and completed in 2000. The initial phases of the research focused on laboratory studies in 1994 and 1995. Pavement tests began in 1995.

VTT has a network of 40 roads throughout the country that have been observed for pavement performance since 1979. An additional 40 test sections are included in the Finnish portion of the SHRP/LTPP study. VTT has suggested that some of the 80 sections could be selected for instrumentation, accompanied by field and laboratory testing, or they would be willing to instrument some test sections on newly built roads.

REFERENCES

AASHTO (1990a) *T 88-90, Particle Size Analysis of Soil.* American Association of State Highway and Transportation Officials, 444 North Capitol Street, N.W., Suite 225, Washington D.C., 20001, AASHTO Materials Part II.

AASHTO (1990b) *T 89-90, Standard Method of Test for Determining the Liquid Limit of Soils.* American Association of State Highway and Transportation Officials, 444 North Capitol Street, N.W., Suite 225, Washington D.C., 20001, AASHTO Materials Part II.

AASHTO (1990c) *T 90-87, Standard Method for Determining the Plastic Limit and Plasticity Index of Soils.* American Association of State Highway and Transportation Officials, 444 North Capitol Street, N.W., Suite 225, Washington D.C., 20001, AASHTO Materials Part II.

AASHTO (1990d) *T 100-90, Standard Method of Tests for Specific Gravity of Soils.* American Association of State Highway and Transportation Officials, 444 North Capitol Street, N.W., Suite 225, Washington D.C., 20001, AASHTO Materials Part II.

AASHTO (1990e) *T 265-86, Standard Method of Test for Laboratory Determination of Moisture Content of Soils.* American Association of State Highway and Transportation Officials, 444 North Capitol Street, N.W., Suite 225, Washington D.C., 20001, AASHTO Materials Part II.

AASHTO (1990f) *T 99-90, Standard Method of Test for the Moisture-Density Relations of Soils Using a 5.5 lb. (2.5 kg) Rammer and a 12 in. (305 mm) Drop.* American Association of State Highway and Transportation Officials, 444 North Capitol Street, N.W., Suite 225, Washington D.C., 20001, AASHTO Materials Part II.

AASHTO (1990g) *T 193-81, Standard Method of Test for the California Bearing Ratio.* American Association of State Highway and Transportation Officials, 444 North Capitol Street, N.W., Suite 225, Washington D.C., 20001, AASHTO Materials Part II.

AASHTO (1990h) *M 145-87, Recommended Practice for the Classification of Soils and Soil-Aggregate Mixtures for Highway Construction Purposes.* American Association of State Highway and Transportation Officials, 444 North Capitol Street, N.W., Suite 225, Washington D.C., 20001, AASHTO Specifications Part I.

Askegaard, V. (1995) Pressure cell calibration tests – Final report. Department of Structural Engineering and Materials, Technical University of Denmark.

Brabston, W.N, W.R. Barker, and G.G. Harvey (1975) Development of a structural design procedure for all-bituminous concrete pavements for military roads. Technical Report S-75-10, U.S. Army Waterways Experiment Station, Vicksburg, Mississippi.

Dawson, A. (1994) *The Emu System Users Manual.*

Dormon, G.M., and C.T. Metcalf (1965) Design curves for flexible pavements based on layered system theory. *Highway Research Record,* No. 71.

Highway Research Board (1962) The AASHO Road Test, Report 5, Pavement Research. Special Report 61E, National Academy of Sciences–National Research Council, Publication No. 954, Washington, D.C.

Hildebrand, G. (1994) Calculation of stresses in the FERF and the RTM: Recommendations for test section construction and laboratory materials characterization. Report 94-11, Cornell Local Roads Program, Cornell University, Ithaca, New York.

Huang, Y.H. (1993) *Pavement Analysis and Design.* Englewood Cliffs, New Jersey: Prentice Hall.

Irwin, L.H., I. Ishibashi, and W. Yang (1985) Validation of the mechanistic approach to nondestructive pavement evaluation for aggregate surfaced roads. Report 85-1, Cornell Local Roads Program, Cornell University, Ithaca, New York.

MacDonald, R., and S. Baltzer (1997) Subgrade performance study, Part 1: Materials, construction, and instrumentation. Report 85P, Danish Road Institute, Roskilde, Denmark.

Patterson, W.D.O. (1972) Measurement of pavement deformation using induction coils. Road Research Unit, National Roads Board, Wellington, New Zealand.

Peattie, K.R. (1965) Design curves for flexible pavements based on layered system theory. Discussion, *Highway Research Record,* No. 71.

Vitel, Inc. (1994) *Hydra Soil Moisture Probe User's Manual.* Version 1.2, Vitel, Inc., 14100 Parke Long Court, Chantilly, Virginia 22021.

Webster, S.L., R.H. Grau, and T.P. Williams (1992) Description and application of dual mass dynamic cone penetrometer. Instruction Report GL-92-3, U.S. Army Waterways Experiment Station, Vicksburg, Mississippi.

Yoder, E.J., and M.W. Witczak (1972) *Principles of Pavement Design.* New York: Wiley and Sons.

Zhang J., and E. Selig (1995) Evaluation of earth pressure cells with vertical and horizontal pressure control. Geotechnical Report No. CRR95-427F, University of Massachusetts, Amherst, Massachusetts.

Zhang J., W. Ebersohn, and E. Selig (1995) Evaluation of earth pressure cells for pavement subgrade performance study. Geotechnical Report No. CRR95-427F, University of Massachusetts, Amherst, Massachusetts.

REPORT DOCUMENTATION PAGE

1. REPORT DATE (DD-MM-YY)	2. REPORT TYPE	3. DATES COVERED (From - To)
March 2003	Technical Report	

4. TITLE AND SUBTITLE

Pavement Subgrade Performance Study: Project Overview

5a. CONTRACT NUMBER

5b. GRANT NUMBER

5c. PROGRAM ELEMENT NUMBER

6. AUTHOR(S)

Vincent Janoo, Lynne Irwin, and Robert Haehnel

5d. PROJECT NUMBER

5e. TASK NUMBER

5f. WORK UNIT NUMBER

7. PERFORMING ORGANIZATION NAME(S) AND ADDRESS(ES)

U.S. Army Engineer Research and Development Center
Cold Regions Research and Engineering Laboratory
72 Lyme Road
Hanover, NH 03755-1290

8. PERFORMING ORGANIZATION REPORT NUMBER

ERDC/CRREL TR-03-5

9. SPONSORING/MONITORING AGENCY NAME(S) AND ADDRESS(ES)

Federal Highway Administration
Washington, DC

Office of the Chief of Engineers
Washington, DC

10. SPONSOR / MONITOR'S ACRONYM(S)

11. SPONSOR / MONITOR'S REPORT NUMBER(S)

12. DISTRIBUTION / AVAILABILITY STATEMENT

Approved for public release; distribution is unlimited.

Available from NTIS, Springfield, Virginia 22161.

13. SUPPLEMENTARY NOTES

14. ABSTRACT

Mechanistic design or evaluation of pavements requires fundamental material properties and material failure criteria as a function of load and environmental effects such as temperature and moisture content. The strength or weakness of a pavement structure is based on the performance of the subgrade. The current subgrade failure criteria used in many mechanistic design/evaluation methodologies were surmised mainly from tests that did not consider the effects of subgrade soil type or moisture content. Because of these limitations the current FHWA-sponsored Subgrade Performance Study was designed to investigate and upgrade the failure criteria of subgrade materials. The project plans to study the effect of subgrade type and moisture content on the failure criteria. This international study includes testing at the U.S. Army Cold Regions Research and Engineering Laboratory, where test sections are being constructed using four subgrade types and three moisture contents and subjected to accelerated loading. The sections are instrumented with stress, strain, moisture, and temperature sensors. In this study the ambient temperature is held at around 20°C. This report provides an overview of the test program and testing procedure. Subsequent reports will detail the construction of each test section, the data acquired, and the results.

15. SUBJECT TERMS

Failure criteria
Pavement

Pavement design
Subgrade

16. SECURITY CLASSIFICATION OF:

a. REPORT	b. ABSTRACT	c. THIS PAGE	17. LIMITATION OF ABSTRACT	18. NUMBER OF PAGES	19a. NAME OF RESPONSIBLE PERSON
U	U	U	U	80	**19b. TELEPHONE NUMBER** (include area code)